water

MDPI

Article

Sustainable Heat Transfer Management: Modeling of Entropy Generation Minimization and Nusselt Number Development in Internal Flows with Various Shapes of Cross-Sections Using Water and Al_2O_3/Water Nanofluid

Atef El Jery [1,2,*], P. Satishkumar [3], Mohammed Abdul Jaleel Maktoof [4], Marian Suplata [5], Branislav Dudic [5,6,*] and Velibor Spalevic [7,8]

1 Department of Chemical Engineering, College of Engineering, King Khalid University, Abha 61421, Saudi Arabia
2 National Engineering School of Gabes, Gabes University, Ibn El Khattab Street, Zrig, Gabes 6029, Tunisia
3 Department of Mechanical Engineering, Study World College of Engineering, Coimbatore 641105, Tamilnadu, India
4 Department of Computer Science, Al-Turath University College, Baghdad 10011, Iraq
5 Faculty of Management, Comenius University Bratislava, 82005 Bratislava, Slovakia
6 Faculty of Economics and Engineering Management, University Business Academy, 21102 Novi Sad, Serbia
7 Biotechnical Faculty, University of Montenegro, 81000 Podgorica, Montenegro
8 Faculty of Philosophy, Geography, University of Montenegro, 81400 Niksic, Montenegro
* Correspondence: ajery@kku.edu.sa (A.E.J.); branislav.dudic@fm.uniba.sk (B.D.)

Abstract: In order to achieve the best performance of a thermal system, two major analyses must be carried out on the system: energy and entropy generation. The best scenario is a mechanism in which the system has minimum entropy generation and the highest *Nu* number. In this regard, we investigated entropy generation and *Nu* number of fluid flow through tubes of various cross-sections, namely circular tubes, square channels, and rectangular ducts. Additionally, the addition of nanoparticles was tested, and both analyses were carried out. The results reveal that using nanoparticles could significantly increase *Nu* number and, at the same time, decrease entropy generation. The results showed that the circular cross-section performs better in *Nu* number and entropy generation. In most cases, the rectangular cross-section performed better than the square one in terms of energy and entropy. In the best case, the average *Nu* for the circular cross-section was 26% greater than that of the square. The average *Nu* of the rectangular cross-section showed that this value is 5% greater than that of the square cross-section. Additionally, the total entropy generation of circular cross-sections, which is the minimum, was 44% and 38% lower than rectangular and square cross-sections, respectively.

Keywords: sustainable management; entropy generation; Nusselt number; nanofluid; experimental study; heat transfer

Citation: Jery, A.E.; Satishkumar, P.; Abdul Jaleel Maktoof, M.; Suplata, M.; Dudic, B.; Spalevic, V. Sustainable Heat Transfer Management: Modeling of Entropy Generation Minimization and Nusselt Number Development in Internal Flows with Various Shapes of Cross-Sections Using Water and Al_2O_3/Water Nanofluid. *Water* **2023**, *15*, 89. https://doi.org/10.3390/w15010089

Academic Editor: Yakun Guo

Received: 5 December 2022
Revised: 17 December 2022
Accepted: 22 December 2022
Published: 27 December 2022

1. Introduction

The sustainable management of natural resources and systems includes exchanges of both matter and energy. Those systems in their surroundings are thermodynamically open and should tend towards a steady state with minimum production of entropy. Entropy is produced in a system and during a process due to irreversibility. Several factors, such as friction, convective heat transfer properties, temperature difference, loss, and the mixture of two substances, cause entropy production. Entropy generation reduces the available work of the system. For this reason, analyzing the second law of thermodynamics, investigating the entropy generation, and minimizing it seem logical [1].

Bejan [2] presented various methods to calculate and minimize local volumetric entropy generation. Additionally, many researchers have studied entropy generation in

different geometries [3–13]. Dalir [14] investigated the entropy generation numerically for forced convection in a non-Newtonian fluid on a tensile sheet. In this research, the Deborah number increased with the increase in entropy production. In Biswal et al. [15]'s study, entropy generation in chambers with convex and concave walls was investigated. The highest heat transfer rate and the lowest entropy production were observed in the chamber with the highest concavity in the wall. In the research of Nazeryan et al. [16], the analysis of entropy production in the Wells turbine by changing the thickness of the blades was performed. The results show that entropy generation has beneficial effects in reducing separation at the blade tip with variable thickness. Delouei et al. [17] studied the thermal effects of multi-walled carbon nanotubes (MWCNT) on a vibrating heat exchanger. They concluded that by using MWCNT under vibration, the heat transfer coefficient would increase by 80.52%. In another study, Delouei et al. [18] studied the effects of nanoparticles on pressure drop and heat transfer coefficient of a turbulent flow. They reported that by utilizing ultrasonic vibration, the negative effects of pressure drop was reduced, and the heat transfer coefficient was improved.

Guo studied the heat transfer in the granular flow around [19]. Noghrehabadi et al. [20] analyzed entropy for nanofluid flowing on a tensile sheet. Increasing heat generation parameters and Brownian motion parameters reduced entropy production in the vicinity of the sheet. In the research of Wang et al. [21], the entropy generation in a square cavity with an irreversible distribution rate was studied. The Bejan number also decreased with the distribution of irreversibility rate and Richardson's number in general. Zhou et al. [22] optimized a heat exchanger by minimizing the entropy production rate. The results show that the lowest entropy production rate occurs when the optimal heat transfer allocation ratio decreases. Falahat et al. [23] studied the entropy production of quasi-plastic nanofluids inside a circular duct. In this research, the total entropy generation decreased at a constant *Re* number by reducing the power law index and duct length values. Additionally, with the increase in wall temperature and volume concentration of nanoparticles, total entropy production increased and decreased, respectively.

Shiravi et al. [24] studied a spiral heat exchanger with carbon black nanofluid. The lowest value of entropy production in the mass was 0.21%, while the *Nu* number had the highest value. Kadivar et al. [25] studied nanofluid flow in a spiral coil tube. Saffarian et al. [26] simulated and studied entropy generation on the intake pipe of the internal combustion engine. The results showed that the entropy production was high in the area where the flow meets the valve and the outlet area. Additionally, changing the turbulence model used did not affect the pressure drop, but it affected the entropy production.

The study of entropy generation is also important in heat exchangers. Heat exchangers utilize various tubes of different cross-sections. Considering heat exchangers' widespread use, improving their performance is important. Some of the ideas proposed to enhance the performance of heat exchangers include the use of fins [27,28], turbulator [29,30], wavy surfaces [31,32], magnetic fields [33–35], vibration [36–38], and twisted tubes [39,40]. Due to their unique geometry, these tubes lead to fluid circulation, which improves fluid mixing and, as a result, increases heat transfer from the wall [41–45].

Some researchers have investigated the hydrothermal characteristics of fluid flow in twisted pipes. Dzyubenko et al. [46] studied twisted tubes on heat transfer coefficient (HTC) and pressure drop of fluid flow on a bunch of twisted tubes. It was seen that replacing the normal tube with a twisted tube leads to a 1.5- to 3.5-fold improvement. Zhang et al. [47] investigated the flow of water inside a twisted two-tube heat exchanger experimentally. Using experimental results, they developed a correlation between HTC and pressure drop. The results showed that the shell and tube side was better for the twisted tube than the normal tube. Qing et al. [48] studied the performance of the twisted tube in the evaporator and concluded that the HTC in the twisted tube was 1.29 to 1.51 times that of the normal tube. Yu et al. [49] investigated the water inside five twisted tubes. The results showed that the HTC of the elliptical twisted tubes was much higher than the normal tube, and the improvement rate decreased with the increase in the tube pitch. The *Nu* number of the

twisted pipe was 1.05 to 1.4 times that of the normal pipe, and the pressure drop of the twisted pipe was 1.1 to 1.4 times that of the normal pipe. Samruaisin et al. [50] studied the simultaneous use of twisted pipe and tape on HTC and water pressure drop.

A group of researchers believe that heat exchangers' low efficiency is due to the low thermal conductivity of the fluids commonly used in the industry for cooling. They proposed to solve this problem by adding fine metal particles and metal oxide. The existing limitations in preparing particles with small dimensions caused some problems. In more detail, the prepared particles were in millimeters or, at most, micrometers. This led to problems such as sedimentation and clumping of particles, blockage of flow paths, and increased pressure drop in heat transfer systems. In 1993, researchers made nanoparticles, and two years later, Choi [51] succeeded in synthesizing stable nanoparticle suspension in liquids. He called this suspension nanofluid and measured its thermophysical properties. The low volume fraction of nanoparticles used and the extremely small size of the particles used helped to eliminate issues such as sedimentation and clumping and lower the costs associated with maintaining and transporting these fluids [52,53].

Additionally, due to the extremely small particle size, there are no issues with wear and damage to systems associated with these particles. Moreover, these particles' comparatively high surface area decreases the effects of fluid and solid imbalance and stabilizes the suspension. Researchers have looked at how well nanofluids cool in various applications, and the major finding is that they perform thermally better than traditional coolers [54,55].

The performance of twisted mini-channels was quantitatively examined by Khoshvaght-Aliabadi et al. [56] to determine how water–aluminum oxide nanofluid affected it. Investigations were conducted into the effects of the cross-section (elliptical, semicircular, square, rectangular, and triangular), twist pitch to channel length ratio, nanoparticle concentration, and *Re* number on the outcomes. The outcomes demonstrated that the tested, twisted channels outperformed all others in thermal performance. Additionally, it was shown that nanofluid only outperforms base fluid hydrothermally at concentrations of 1%. The cooling performance of an aluminum oxide water nanofluid flowing in a spiral-twisted tube was numerically examined by Feizabadi et al. [57]. Investigations were conducted on how spiral pitch, twist pitch, and nanoparticle concentration affected the outcomes. According to the findings, raising the nanoparticle concentration raises the *Nu* number but has no impact on the friction coefficient. Using a mixed two-phase model, Omidi et al. [58] numerically examined the turbulent flow of aluminum oxide water nanofluid within a twisted triangular tube fitted with a Y-shaped turbulator. Investigations were conducted on how *Re* number and nanoparticle concentration affected the outcomes. The findings showed that when the *Re* number rises, the *Nu* number ratio of the twisted pipe to the smooth pipe falls.

Additionally, it was shown that raising the nanoparticle concentration causes the *Nu* number to rise but has no influence on the *Nu* number. The heat transmission of aluminum oxide nanofluid inside the square channel was numerically examined by Mahato et al. [59]. They investigated the impacts of *Re* number and nanoparticle concentration on the outcomes. It has been seen that the *Nu* number rises when the twist pitch is reduced, and the Prandtl number rises.

The first law of thermodynamics functionally describes the amount of heat transferred between fluids and the surrounding environment and deals with the quantitative balance and relationships between them [60]. Nevertheless, basic issues such as system efficiency, energy dissipation, entropy production, and irreversibility are related to the second law of thermodynamics. In fact, to achieve accurate and practical efficiencies of real thermodynamic systems, the second law is a practical principle. It enables obtaining thermal and mechanical energies and their relationship [61,62]. Therefore, it is necessary to present both energy and entropy generation analysis of a thermal system to achieve proper efficiency [63,64].

In the present study, an experimental study of laminar flow in a tube with three cross-sections was carried out. The flow's thermal performance and entropy generation

for water and nanofluids are presented here. Tubes with circular, square, and rectangular cross-sections were studied with various fluids (water and volumetric 1%, 2%, 3%, and 4% nanofluids). The average *Nu* numbers of all cases in four *Re* numbers were studied, and the addition of nanoparticles was also investigated. Moreover, the average *Nu* number was studied in all cases. Plus, the total entropy generation of all cases is compared here, and finally, the case with the best performance is selected.

2. Materials and Methods

2.1. Experimental Setup

The setup's design is based on earlier investigations and comprises several mechanical, electrical, and control components. A schematic representation of the experimental setup employed in this investigation is shown in Figure 1. The test may also be applied in many fluid flow scenarios and boundary situations. Different cross-sections are used for this study, namely circular, square, and rectangular cross-sections. The characteristics of these cross-sections are indicated in the Table 1. The hydraulic diameter of all cross-sections is identical.

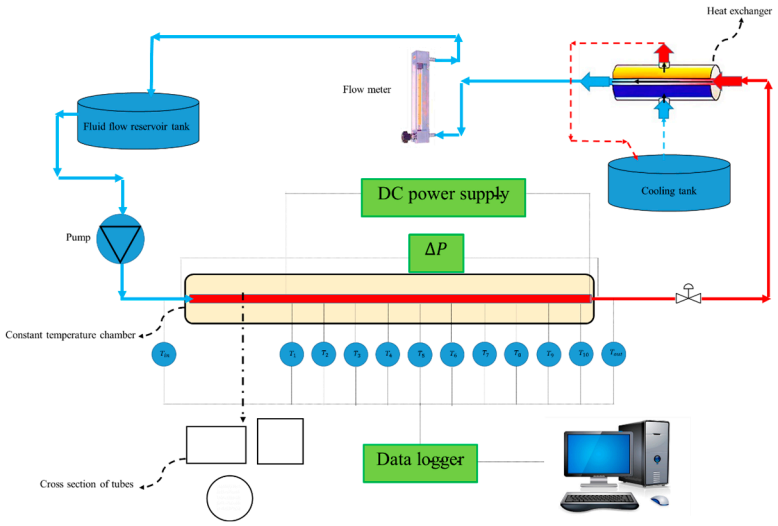

Figure 1. The schematic visualization of the experimental setup.

Table 1. The dimensions of different cross-sections.

Cross-Section	2a	2b	2b/2a	Dh
Circular	-	-	-	0.0154
Square	0.0154	0.0154	1	0.0154
Rectangular	0.0231	0.01155	0.5	0.0154

The flow was established using a copper pipe with dimensions of 2700 mm in length and 15.4 mm in inner diameter, which was chosen to generate a hydrodynamically developed flow. Heat wires with fixed and particular resistance wrapped around the pipe with uniform density are used to generate heat flux, and a DC power source is utilized to apply the required current and voltage to the wires. Direct current is used because there are no variations in this form of electric current, which improves computation accuracy.

A pump is utilized to produce flow in the system, and the fluid storage tank is built of aluminum. The flow rate of the passing fluid is regulated using a flowmeter (measuring range of 0 to 70 L per hour and precision of 1 L per hour), and two separate techniques are employed to maintain the temperature of the incoming fluid tank to the pipe. The initial mechanism is a heat exchanger attached to a sizable tank, and three controlled cooling elements are then employed and attached to the aluminum wall of the storage tank. The heated fluid enters a shell heat exchanger through a tube while being heated by heat flux.

The storage tank is connected to the fan, triggered when the fluid within the tank's fluid temperature rises and runs until it reaches the target temperature. Each cooling element is also connected to heat well. The heat flux is equal to 1500 W/m^2, and it is exerted on a 154 cm length.

The temperature of the fluid entering and leaving a copper pipe is measured by two RTD-type temperature sensors, which have a measurement range of 0 to 200 with an accuracy of 0.1 °C. Furthermore, the wall temperature of copper pipes at a distance of 15 cm between them was measured using 10 K-Type sensors with a measurement range of 0 to 120 and an accuracy of 0.1 °C. The K-Type thermocouple was chosen because it has a smaller measuring probe than other thermocouples, which results in improved accuracy.

Temperature sensors are connected to the data logger, which then connects to the computer. The computer then manages the findings. To detect the pressure drop in the fluid flow inside the pipe, differential pressure transmitters with a measurement range of 0 to 100 and an accuracy of 0.1 mm are utilized. To stop heat loss, thermal insulation is used to insulate the full length of the pipe.

A negligible effect of less than 0.1 percent has been observed and reported after using two computational and experimental methods to control and evaluate the impact of temperature increase on the amount of electrical resistance and flux passing through it from the beginning to the end of the heating wire.

Using the relationship in the laminar flow, the length of 105 cm at the beginning of the pipe without applying heat flux is taken into consideration in order to achieve and ensure the development of the fluid flow as well as to obtain the ability to evaluate the calculations with the existing equations. The research of the thermal developing zone is taken into account in this study in order to precisely analyze the influence of the type of heat flux application. Additionally, the functioning accuracy of all measuring instruments and displays has been guaranteed by calibration before and after the testing.

2.2. Nanofluid Preparation

There are two ways to prepare nanofluids: the one-step method and the two-step method. In the first technique, the fluid serves as the nanoparticle source. The latter approach, however, disperses nanoparticles in the fluid as dry particles. The first technique has the advantage that nanoparticle size and distribution can be regulated, and nanofluid stability is greater in this method than in the two-step method. The following presents how a one percent weight fraction nanofluid was produced. The nanoparticle properties are shown in the Table 2.

Table 2. Thermophysical properties of a nanoparticle.

ρ_p(kg/m^3)	Cp_p (j/kgK)	K_p (w/mK)	d_p (nm)
3690	880	18	15

To manufacture the nanofluids for this investigation, 25 nm $\gamma - Al_2O_3$ nanoparticles (produced by Nanostructured & Amorphous Materials Inc., Houston, TX, USA) were used. Density $\rho_s = 3700$ kg/m^3, heat capacity $C_{p,s} = 880$ J/kg K, and thermal conductivity $k_s = 46$ W/m K are the characteristics of nanoparticles. These physical characteristics of the nanoparticle were extracted from the datasheet provided by the manufacturer. No stabilizer or dispersant was utilized in the current investigation. This is because the addition of any substance has the potential to alter the fluid's characteristics. The features of heat transmission in laminar flow were studied using nanofluids with various concentrations of $\gamma - Al_2O_3$ nanoparticles. Nanoparticles were combined with distilled water in a flask using the appropriate amount of powder and the corresponding weight of the solid and then vibrated for 6–12 h using an ultrasonic mixing device (Panasonic 3600S, 150 W). After 12 h of repose, no sedimentation was seen for any volume fractions. However, partial deposition of $\gamma - Al_2O_3$ nanoparticles, including a 4 percent volume component in water,

was seen during the test (4–5 h). Another practical issue is how to prepare nanofluids that are more stable for use in engineering applications.

The addition of nanoparticles would ameliorate the thermal performance of the base fluid in two main ways. First, since the nanoparticles are mainly metallic, they have high thermal conductivity. Therefore, adding these nanoparticles would enhance the thermal properties of the base fluid. Moreover, by adding nanoparticles, the wettability of the fluid would increase, so higher amounts of heat could be dissipated from the surface using the nanofluid.

3. Governing Equations

3.1. Thermophysical Properties of Nanofluid

A Transient Hot Wire (THW) was utilized to test the conductivity of the nanofluid. A KD2 Pro Thermal Property Analyzer was used to test the thermal conductivity of nanofluids. It is made up of sensor needles and a wearable microcontroller. Three distinct temperatures were used for each measurement. We checked our results with the thermal conductivity of glycerol supplied by the supplier's reference samples in order to confirm the precision of our findings. Additionally, a Brookfield LVDV III Rheometer was used to test the dynamic viscosity of nanofluids. The same method of viscosity verification is utilized. When the measurements' results are compared to well-known formulae, the results line up.

The base fluid's thermophysical characteristics might alter when nanoparticles are added. We must thus devise a mechanism to determine the effective parameters. The following formulas are used to compute density, specific heat, thermal conductivity, and dynamic viscosity:

$$\rho_{nf} = (1-\varphi)\rho_w + \varphi\rho_s \tag{1}$$

$$C_{p,nf} = \frac{(1-\varphi)\rho_w C_{p,w} + \varphi\rho_s C_{p,s}}{\rho_{nf}} \tag{2}$$

where the concentration of nanoparticles is φ. Base fluid, nanofluid, and particle are indicated by the subscripts w, nf, and p, respectively.

3.2. Energy Analysis Equation

Equation (5) may be used to electrically compute the quantity of heat flux that penetrates the copper tube's outer surface through the heating wire in the flux application area.

By measuring the mass flow rate with a flow meter, determining the fluid's inlet and outlet temperatures using the knowledge that it is in the flow path, and inserting the appropriate value for the specific heat capacity from Equation (4), it is possible to determine the amount of flux that the fluid has received.

$$q^{''}_{el} = \frac{VI}{A_P} \tag{3}$$

$$q^{''}_{th} = \frac{\dot{m}C_p(T_{m,out} - T_{m,in})}{A_P} \tag{4}$$

In these equations, $q^{''}_{el}$ and $q^{''}_{th}$ are, respectively, the amount of flux exerted and received by the fluid. I is the electrical current, and V is the voltage. $\dot{m}$ is the mass flow rate, and A_P is the surface on which heat is supplied. The specific heat capacity is C_p, and bulk fluid temperature (T_m) at the intake and outflow are denoted by out and in subscripts, respectively.

Therefore, the difference between the applied electrical heat flux and the heat flux received by the fluid is used to compute the amount of heat loss on the insulating side, known as $q^{''}_{loss}$ [65].

$$q^{''}_{loss} = q^{''}_{el} - q^{''}_{th} \tag{5}$$

In this study, the amount of heat loss has been calculated to be no more than 6%, using both experiments and Equation (5). As a consequence, the effectiveness of the insulating work is guaranteed.

Equation (6) provides the average temperature of the fluid volume at any distance from the pipe's entrance. Using Equation (7), the HTC is determined using the average temperature of the fluid volume and the temperature recorded by the temperature sensors attached to the copper pipe's wall [65].

$$T_m(x) = \frac{q_{th}^{''} Px}{\dot{m} C_p} + T_{m,in} \tag{6}$$

$$q^{''} = h(x)(T_s(x) - T_m(x)) \tag{7}$$

P stands for the pipe cross-periphery, x for the longitudinal component, h for the convective HTC, and T_s is for the temperature of the pipe surface in these equations.

The pipe is copper, with high conductivity and a wall thickness of only 0.9 mm. As a result, the temperature difference between the pipe's inner and outer walls is very small—less than 0.01 degrees Celsius, according to calculations. It is possible to guarantee that the temperature of the pipe's outside and inner walls are almost identical. Equation (8) is used to compute the local Nu at any distance from the tube's start, and Equation (9) is used to obtain the average value of the convective HTC [65].

$$Nu(x) = \frac{h(x) D_h}{K} \tag{8}$$

$$h_{ave} = \frac{1}{l} \int_0^l h(x) dx \tag{9}$$

In this equation, D_h stands for the hydraulic diameter, K for the fluid's thermal conductivity, and l for the pipe's length.

3.3. Energy Analysis Equation

Entropy generation depends on two separate factors, thermal and frictional, when it comes to the volume of the copper pipe [2,66].

$$S_{gen,T} = S_{gen,t} + S_{gen,f} \tag{10}$$

The non-dimensional Bejan number (Be) is used to assess the significance of each of these concepts.

$$Be = \frac{S_{gen,t}}{S_{gen,f}} \tag{11}$$

The Be number, which ranges from 0 to 1, is used to indicate whether the thermal or frictional flow is more prevalent. According to [67], the entropy generation is calculated as follows:

$$S_{gen,t} = \frac{q^2 \, P \, D_h \, L}{Nu \, k_{nf} \, T_{ave}} \tag{12}$$

$$S_{gen,f} = \frac{2 \, m^3 \, f \, L}{\rho \, T_{ave} \, D_h \, A_c^2} \tag{13}$$

As a result, the formulation for the total entropy generation is:

$$S_{gen,T} = \frac{q^2 \, P \, D_h \, L}{Nu \, k_{nf} \, T_{ave}} + \frac{2 \, m^3 \, f \, L}{\rho \, T_{ave} \, D_h \, A_c^2} \tag{14}$$

Two geometry-related parameters, namely P and A_c, are calculated for each cross-section. In Equation (15), T_{ave} is calculated as:

$$T_{ave} = \frac{T_{in} - T_{out}}{\ln\left(\frac{T_{in}}{T_{out}}\right)} \tag{15}$$

In addition, to calculate T_{out}, we use the following:

$$T_{out} = T_{in} + \frac{qA_s}{mC_p} \tag{16}$$

The friction factor for the laminar flow is calculated from Equation (17).

$$f = \frac{64}{Re} \tag{17}$$

Entropy production in a laminar flow with a circular cross-section is estimated using the formulae mentioned above.

4. Uncertainty Analysis

Uncertainty analysis was conducted to determine the error rate of measuring equipment and the cumulative effect of these errors on the parameters effective in measuring the fluid flow in this research. Data from the Table 3 shows the uncertainty of measurement in the equipment.

Table 3. The equipment's information and uncertainty.

Equipment	Measurement Range	Minimum Measuring Value	The Studied Range in the Present Study	Uncertainty Percentage
K-Type thermocouple	0–120 (°C)	0.1	24.5–38.5	0.260
RTD-Pt100 thermocouple	0–200 (°C)	0.1	25.5–34.5	0.290
Voltmeter	0–100 (V)	0.01	24–48	0.021
Ampere meter	0–10 (A)	0.001	0.85–1.2	0.083
Ohmmeter	0–100 (Ω)	0.001	27.4–54.5	0.002
Pressure transducer	0–100 (mbar)	0.1	8.5–45	0.222
Flow meter	0–70 (L/min)	1	10–60	1.667
Geometrical dimensions	1–20 (mm)	0.1	1–20	0.500
Physical properties	-	-	-	0.100

The uncertainty calculation relations for a parameter such as the Nu number are as follows [68].

$$\delta Nu = \sqrt{\left(\frac{\partial Nu}{\partial h}\delta h\right)^2 + \left(\frac{\partial Nu}{\partial D}\delta D\right)^2 + \left(\frac{\partial Nu}{\partial K}\delta K\right)^2} \tag{18}$$

Then, to calculate the percentage of uncertainty, we have:

$$\frac{\delta Nu}{Nu} = \sqrt{\left(\frac{\delta h}{h}\right)^2 + \left(\frac{\delta D}{D}\right)^2 + \left(\frac{\delta K}{K}\right)^2} \tag{19}$$

In the same way, we have various parameters such as HTC, heat flux q'', friction coefficient f, and Reynolds Re [68]:

$$\frac{\delta h}{h} = \sqrt{\left(\frac{\delta q''}{q''}\right)^2 + \left(\frac{\delta T_s}{T_s - T_b}\right)^2 + \left(\frac{\delta T_b}{T_s - T_b}\right)^2} \tag{20}$$

$$\frac{\delta q''}{q''} = \sqrt{\left(\frac{\delta V}{V}\right)^2 + \left(\frac{\delta I}{I}\right)^2} \tag{21}$$

$$\frac{\delta f}{f} = \sqrt{\left(\frac{\delta(\Delta P)}{\Delta P}\right)^2 + \left(\frac{\delta L}{L}\right)^2 + \left(\frac{\delta D}{D}\right)^2 + \left(\frac{\delta \rho}{\rho}\right)^2 + \left(\frac{2\delta v}{v}\right)^2} \tag{22}$$

$$\frac{\delta Re}{Re} = \sqrt{\left(\frac{\delta v}{v}\right)^2 + \left(\frac{\delta d}{d}\right)^2 + \left(\frac{\delta v}{v}\right)^2} \tag{23}$$

In these equations, T_s is the temperature of the pipe surface, ΔP is the pressure drop, ρ is the density, and V is the voltage. Table 4 presents the percentage of uncertainty in calculating parameters considering the above relationships in the current research.

Table 4. The uncertainty of the parameters.

Parameter	Uncertainty Percentage
q	0.086
h	0.091
Nu	0.518
Re	1.746
f	1.827

5. Data Collection and Validation

Validation of the Experimental Setup

The various components of the experimental apparatus were checked and calibrated accurately before the tests began, and then the equipment was connected. After ensuring the experimental setup was stable, more measurements were taken and recorded on the computer.

The data collector reports the temperature of the copper tube wall using K-Type temperature sensors. Then, Equation (6) is used to determine the bulk temperature of the fluid at each location. The HTC is first determined using Equation (7), and the local Nu number is then stated with respect to the dimensionless length using Equation (8). To assure repeatability, each experiment was run at least three times.

The well-known correlation of Shah and London has been applied for the growing heat transfer in the hydrodynamically formed flow in the tube in order to assess the early findings for the water with constant heat flux.

$$Nu_{x^*} = \begin{cases} 1.302x^{*-\frac{1}{3}} - 1 & x^* \leq 0.00005 \\ 1.302x^{*-\frac{1}{3}} - 0.5 & 0.00005 < x^* < 0.0015 \\ 4.364 + 8.68\left(10^3 x^*\right)^{-0.506} e - 41x^* & x^* > 0.0015 \end{cases} \tag{24}$$

In this relation, x^* is the dimensionless length and is defined as follows:

$$x^* = \frac{\frac{x}{D}}{Re_D Pr} \tag{25}$$

Figure 2 shows the measurements' findings and the HTC comparisons with Shah and London's correlation. It should be noted that in the validation case, the heat flux is 1400 W/m^2.

The highest error with the analytical values derived using Shah and London's equation in four Re numbers is 5%, as shown in the figure. The experimental and analytical findings agree satisfactorily. It has been noted that the outcomes are satisfactory.

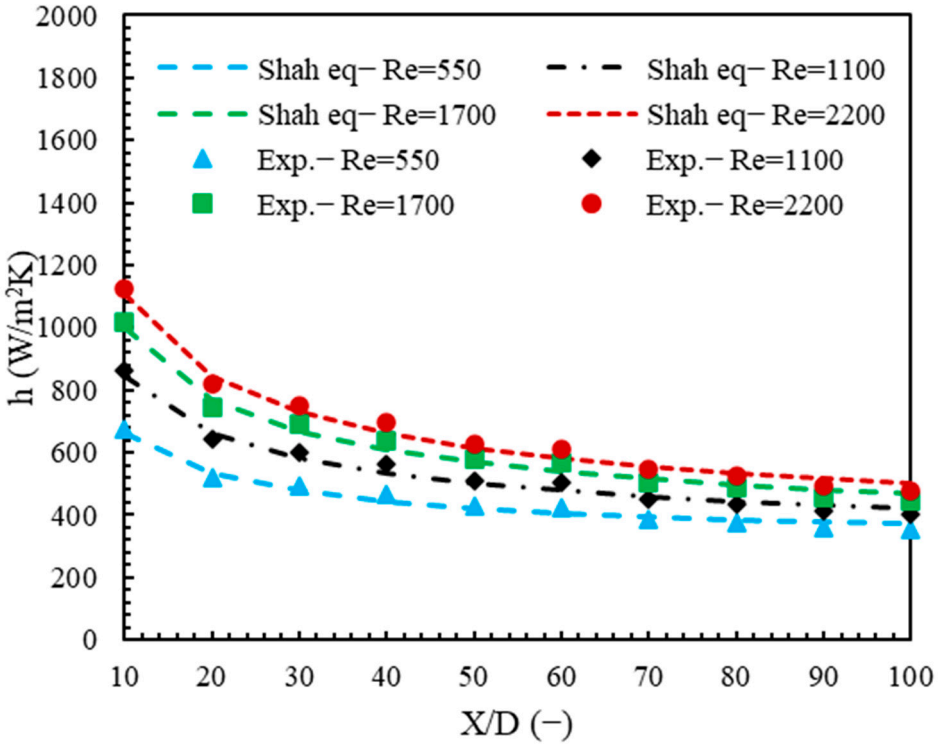

Figure 2. The validation of the experimental data with the analytical results for h.

6. Results and Discussion

The examination of the energy and entropy generation in water and nanofluid in all cross-sections is described in the following section. Additionally, the impacts of *Re* number, nanoparticle addition, and cross-sectional shape are investigated.

6.1. Energy Analysis

The impact of using different cross-sections is considered in the present study. The effects of *Re* number and nanoparticle addition are studied in this study. The local and average *Nu* numbers are studied in all cross-sections, and the best choice is selected. The energy analysis assesses the thermal efficiency of the fluid flow. The average and the local *Nu* numbers are analyzed and contrasted in this situation. In the last part, the ideal example is chosen. The impacts of Re and nanoparticle concentration are explored. The higher *Nu* number for the circular cross-section is attributed to the decrease in the boundary layer. The boundary layer plays a major role in the thermal performance of the problem. The enhancement of thermal conductivity caused by the addition of nanoparticles is also investigated and referred to in the analyses.

Figure 3 shows the water results in different cross-sections with a variety of *Re*. Figure 3a shows the local *Nu* number for water in $Re = 850$. It is obvious that *Nu* is higher at the beginning of the tube, and it gradually decreases and levels off. The circular cross-section's *Nu* is higher than the rest along the tube. The rectangular tube has higher *Nu* when compared to square tubes. By increasing the *Re*, the *Nu* increases as well, and a similar trend is observed, according to Figure a–d. At the beginning of the tube, the *Nu* of the circular cross-section is 27.03%, 32.52%, 36.74%, and 41.98% higher than that of the square cross-section in the designated *Re* numbers, respectively. The same values for the rectangular cross-section compared to the square are 2.52%, 2.16%, 1.92%, and 1.57%, respectively. However, this difference decreases as the flow reaches the end of the tube, dropping to less than 21% in the circular cross-section compared to the square cross-section. This is because the flow is fully developed towards the end of the tube, and they reach their constant values, which are at around the same range. Moreover, the thickness of the

thermal boundary layer at the beginning of the tubes differs with their cross-sections due to the mentioned factor.

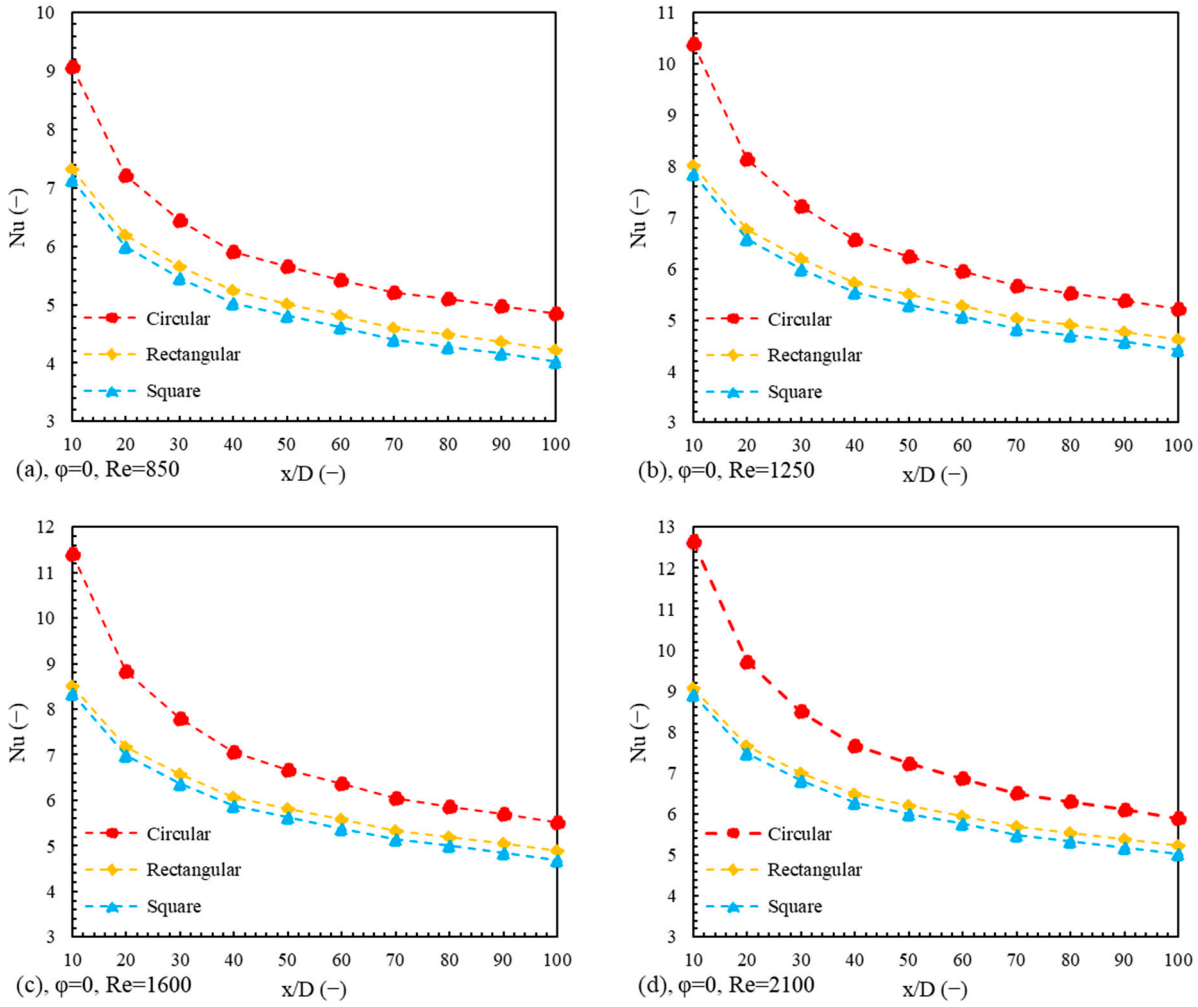

Figure 3. Local *Nu* of water with different cross-sections in (**a**) *Re* = 850, (**b**) *Re* = 1250, (**c**) *Re* = 1600, and (**d**) *Re* = 2100.

Figure 4 shows Nu_{loc} for 1% nanofluid.

Comparing the results of nanofluid to water in Figure 3 an improvement is observed in the *Nu* number. In $Re = 850$, the *Nu* number is improved by 4.2%. This is repeated for $Re = 1250$ where *Nu* for nanofluid is 4.1% higher than that of water. The observed trend in water is seen in nanofluid, where the *Nu* decreases along the tube, and the circular cross-section proves to be the best choice.

Figure 5 shows the results of Nu_{loc} for 2% nanofluid. In this case, a further increase in *Nu* is observed. Compared to water, the *Nu* of 2% nanofluid is 12.8% higher than the *Nu* of water. Therefore, adding nanoparticles, as expected, would increase the thermal performance. This is due to the nanoparticles' high thermal conductivity compared to the base fluid. The maximum *Nu* number is at the beginning of the tube, and it eventually steadily drops throughout the tube length. Like water, by increasing the *Re* number, the thermal performance increases, and the *Nu* number rises. The highest *Nu* number is observed in $Re = 2100$, based on Figure 5d.

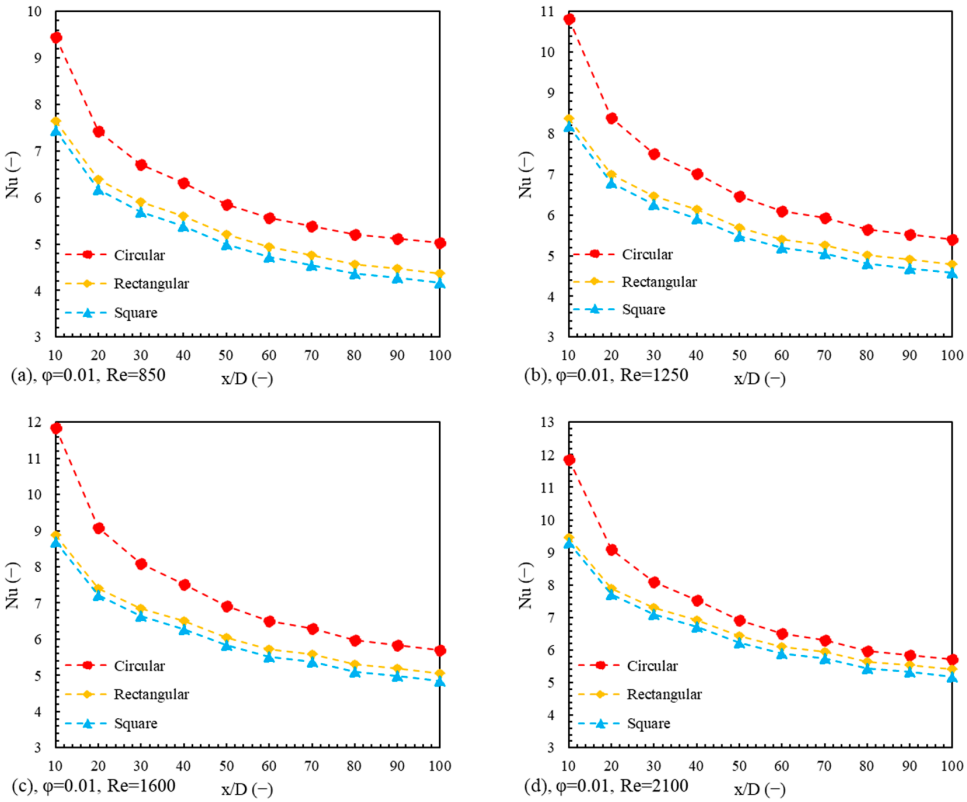

Figure 4. Local *Nu* of 1% nanofluid with different cross-sections in (**a**) *Re* = 850, (**b**) *Re* = 1250, (**c**) *Re* = 1600, and (**d**) *Re* = 2100.

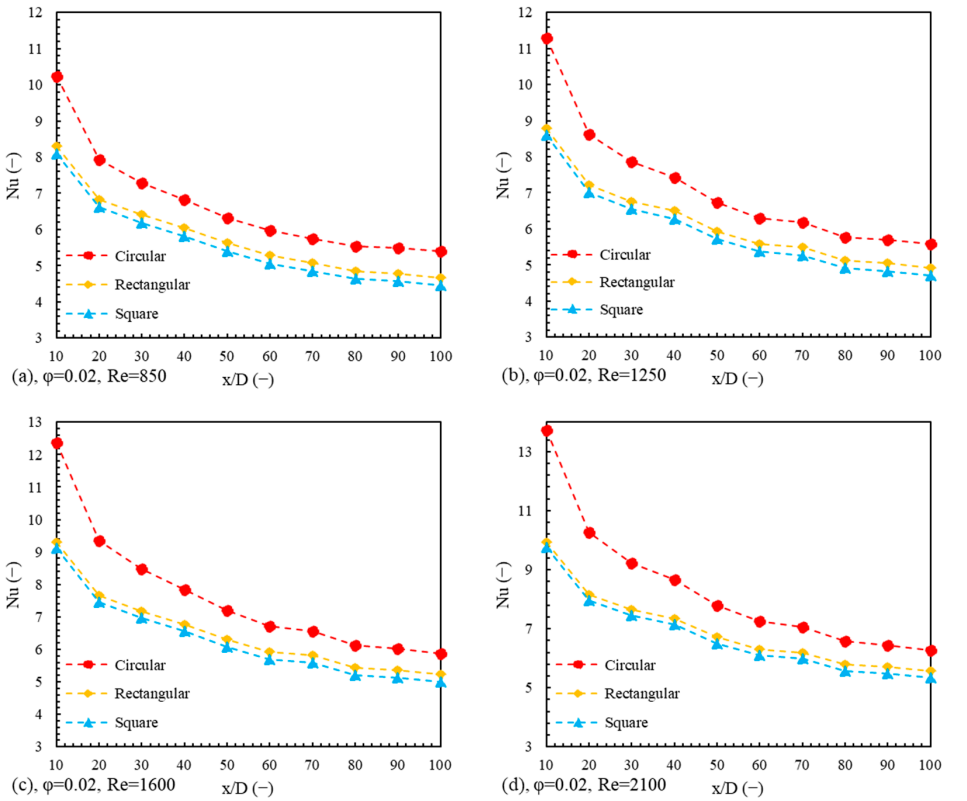

Figure 5. Local *Nu* of 2% nanofluid with different cross-sections in (**a**) *Re* = 850, (**b**) *Re* = 1250, (**c**) *Re* = 1600, and (**d**) *Re* = 2100.

Figures 6 and 7 and present the results for 3% and 4% nanofluid, respectively. These two figures also present increments in *Nu* number compared to more dilute nanofluids and water. Figure 6 shows a marginal improvement of 9.2% along the tube. The same comparison for the nanofluid with 0.04 nanoparticle concentration is made, and the results show an average 7% growth in *Nu*, compared to water, based on Figure 7. A similar trend is observed in all cases, where circular cross-section proves to perform the best at 15% and 20% compared to rectangular and square cross-sections, respectively. In $Re = 2100$, the maximum *Nu* numbers, which are at the beginning of the tube, are equal to 14.26 for 3% nanofluid and 14.09 for 4% nanofluid, according to Figures 6d and 7d. Based on the results of Figures 2–5, the highest values of all three cross-sections in $Re = 850$ and $Re = 1250$ are observed in the nanofluid with 2% nanoparticle concentration. Nevertheless, as the *Re* number increases, the nanofluid with higher nanoparticle concentration has the maximum. That is why in $Re = 1600$ and $Re = 2100$, the maximum *Nu* numbers are measured in nanofluid with 4% nanoparticle concentration.

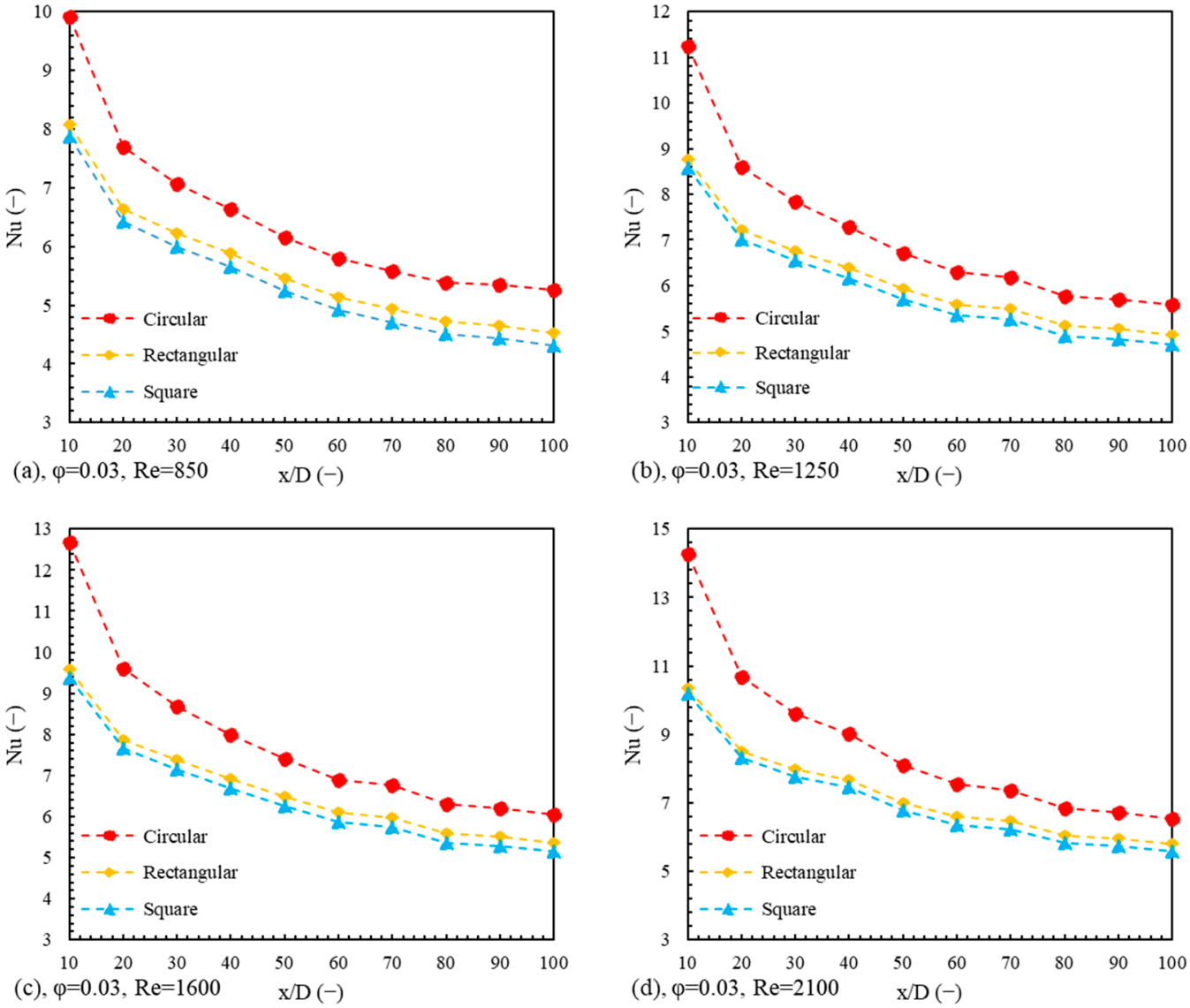

Figure 6. Local *Nu* of 3% nanofluid with different cross-sections in (**a**) $Re = 850$, (**b**) $Re = 1250$, (**c**) $Re = 1600$, and (**d**) $Re = 2100$.

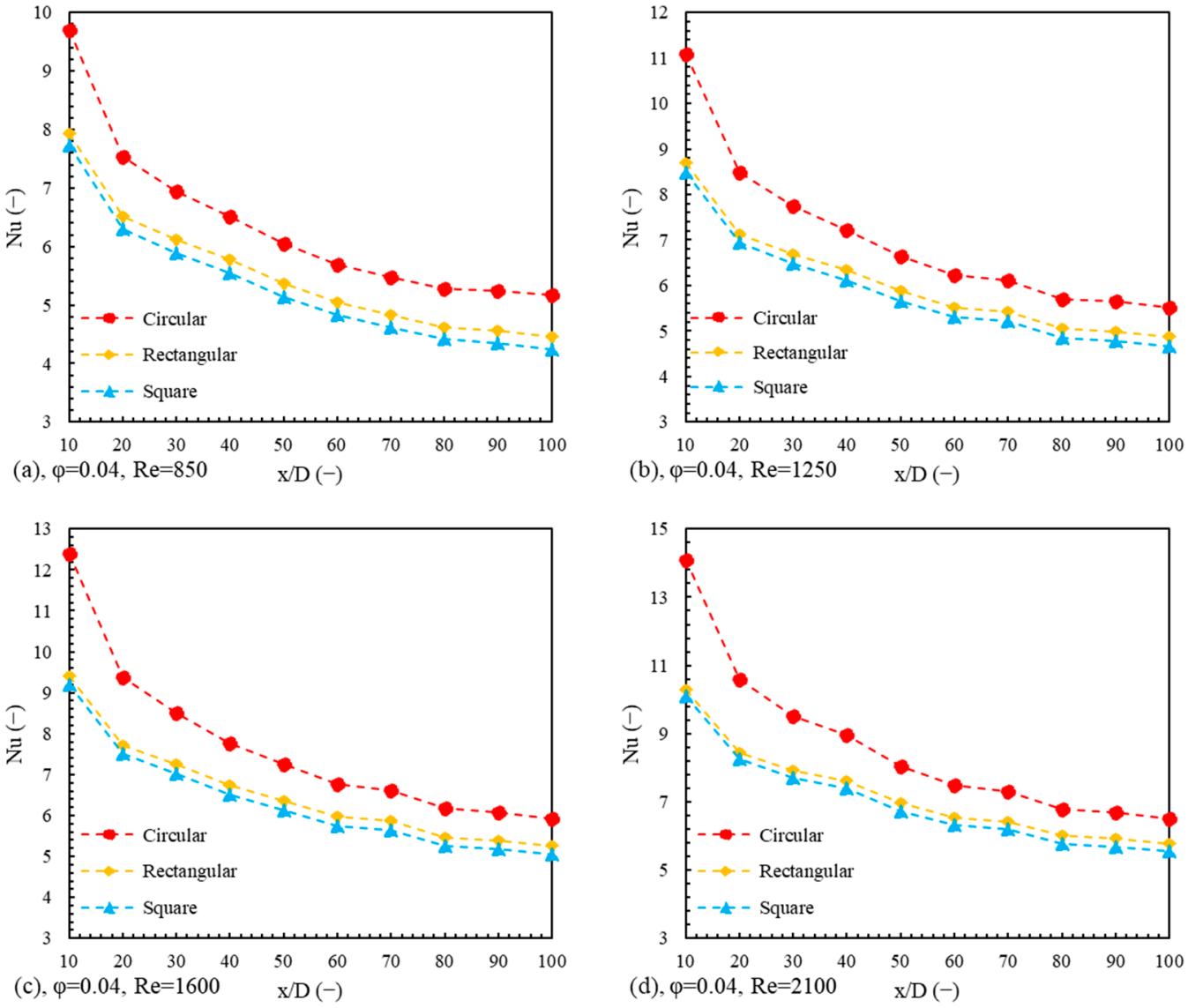

Figure 7. Local *Nu* of 4% nanofluid with different cross-sections in (**a**) $Re = 850$, (**b**) $Re = 1250$, (**c**) $Re = 1600$, and (**d**) $Re = 2100$.

6.1.1. Circular Cross-Section

Figure 8 shows the results of the local *Nu* number in four *Re* numbers in all fluids. As was mentioned in the previous sections, the highest *Nu* number is achieved with 2% nanoparticle concentration in $Re = 850$ and $Re = 1250$. However, in the other two *Re* numbers, the 4% nanoparticle concentration seems to have the maximum amount. The physical justification of the mentioned trend is probably that since in lower *Re* numbers, the possibility of nanoparticle deposition is high, by adding more nanoparticles, the thermal performance decreases. Additionally, the migration of the nanoparticles could impact the results. The thermal conductivity of nanoparticles could enhance the thermal performance, but this also could cause an increase in the thermal boundary layer. The HTC is inversely proportional to the thickness of the thermal boundary layer, and this increase would deteriorate the *Nu* number, as could be observed in Figure 8a,b. Moreover, utilizing nanofluids proved to enhance thermal performance because, in all cases, the measured *Nu* number for nanofluids is higher than that of water.

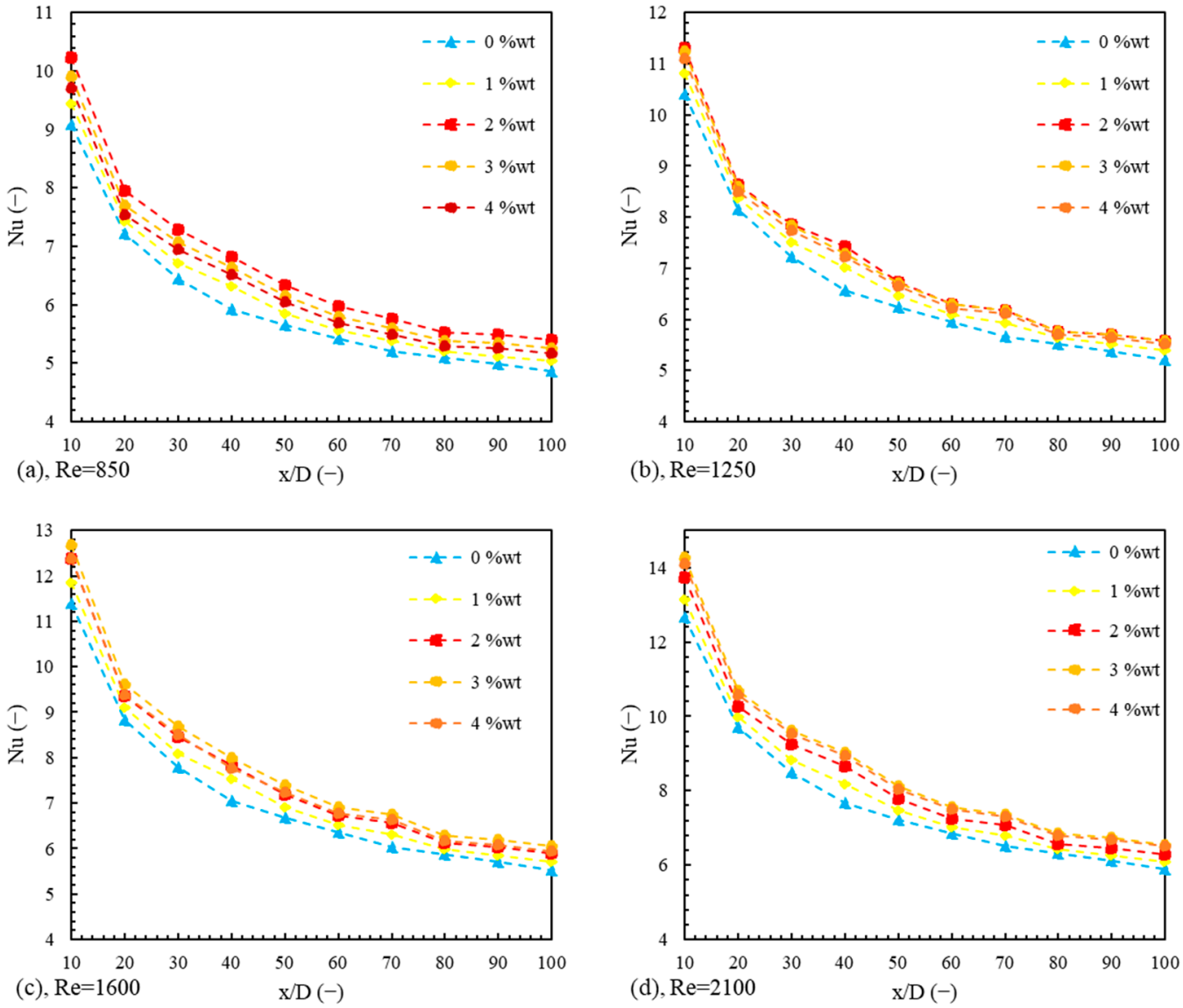

Figure 8. The results of local *Nu* for circular cross-section with different nanoparticle concentrations in (**a**) *Re* = 850, (**b**) *Re* = 1250, (**c**) *Re* = 1600, and (**d**) *Re* = 2100.

6.1.2. Square Cross-Section

The square cross-section has the lowest heat transfer rate among the three examined cross-sections. As seen in the circle section, the amount of heat transfer also increases with the increase in the *Re* number. As a result, the highest value of the *Nu* number can be seen in Figure 8d. Due to the completion of the boundary layer and the development of the fluid flow along the tube, we also see a decrease in the value of the *Nu* number. The effect of adding nanoparticles to the base fluid has also been investigated in Figure 9. The results show that the highest value of *Nu* number in the nanofluid has 2% nanoparticles, just like the circular section at *Re* numbers 850 and 1250. In *Re* numbers 1600 and 2100, the best result is observed in 4% nanofluid. It should be noted that the values of the *Nu* number in the square cross-section are 15–20% less than in the circular cross-section. As a result, in the square section, the best condition was observed at *Re* number 2100 and nanofluid with 4% concentration.

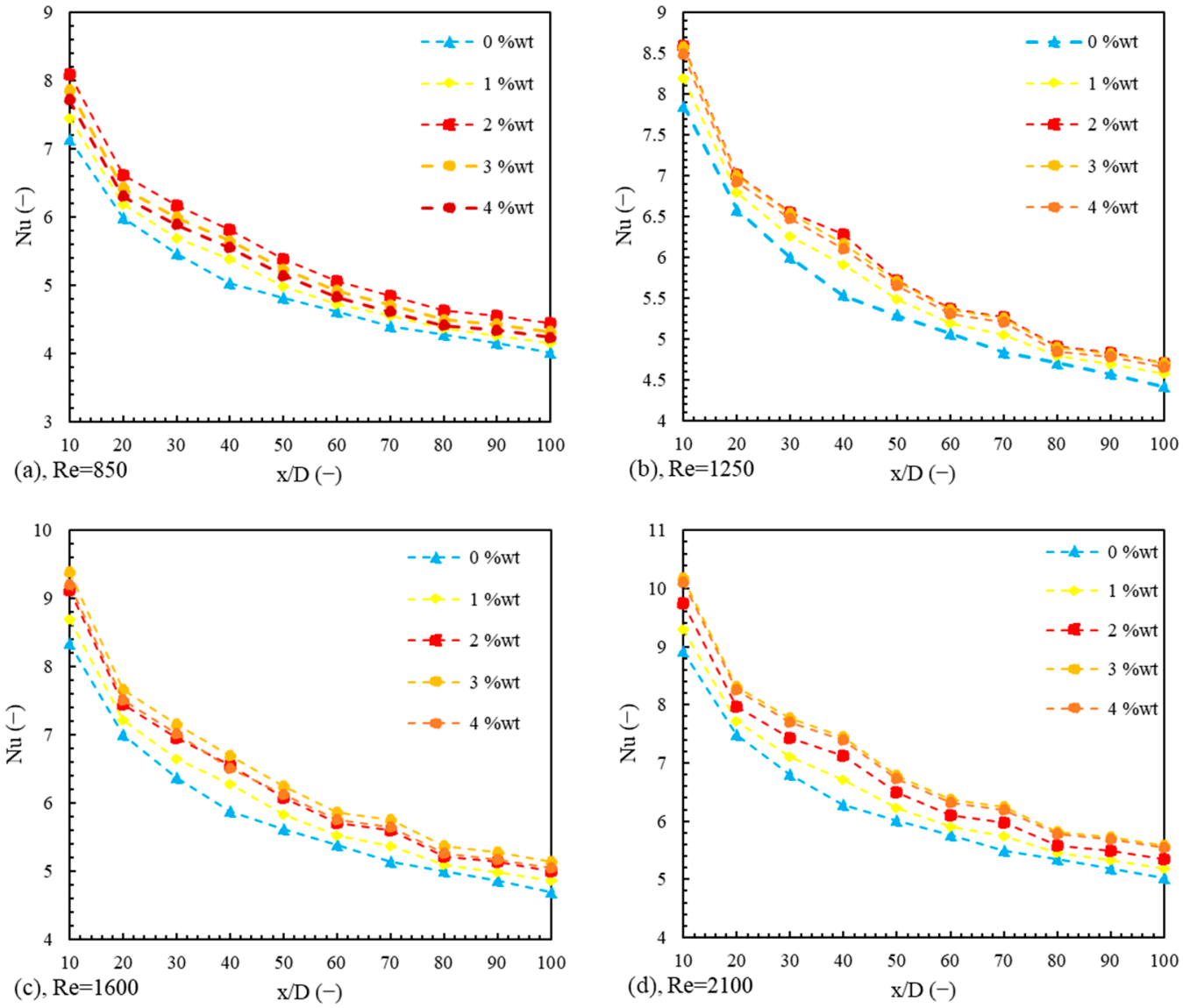

Figure 9. The results of local *Nu* for square cross-section with different nanoparticle concentrations in (**a**) *Re* = 850, (**b**) *Re* = 1250, (**c**) *Re* = 1600, and (**d**) *Re* = 2100.

6.1.3. Rectangular Cross-Section

According to Figure 10, it can be seen that, like the other two sections, the *Nu* number decreases due to the fact that the hydrodynamic boundary layer is developed along the tube. In two lower *Re* numbers, i.e., 850 and 1250, the highest value of *Nu* number is observed in nanofluid with 2% concentration. However, at *Re* numbers 1600 and 2100, nanofluid with 4% concentration has the highest *Nu* number. In general, adding nanoparticles to the base fluid improves the system's thermal performance, and this improvement has different values in different situations. As a result, the effective factors in the *Nu* number are cross-sectional geometry, *Re* number, and nanoparticle concentration.

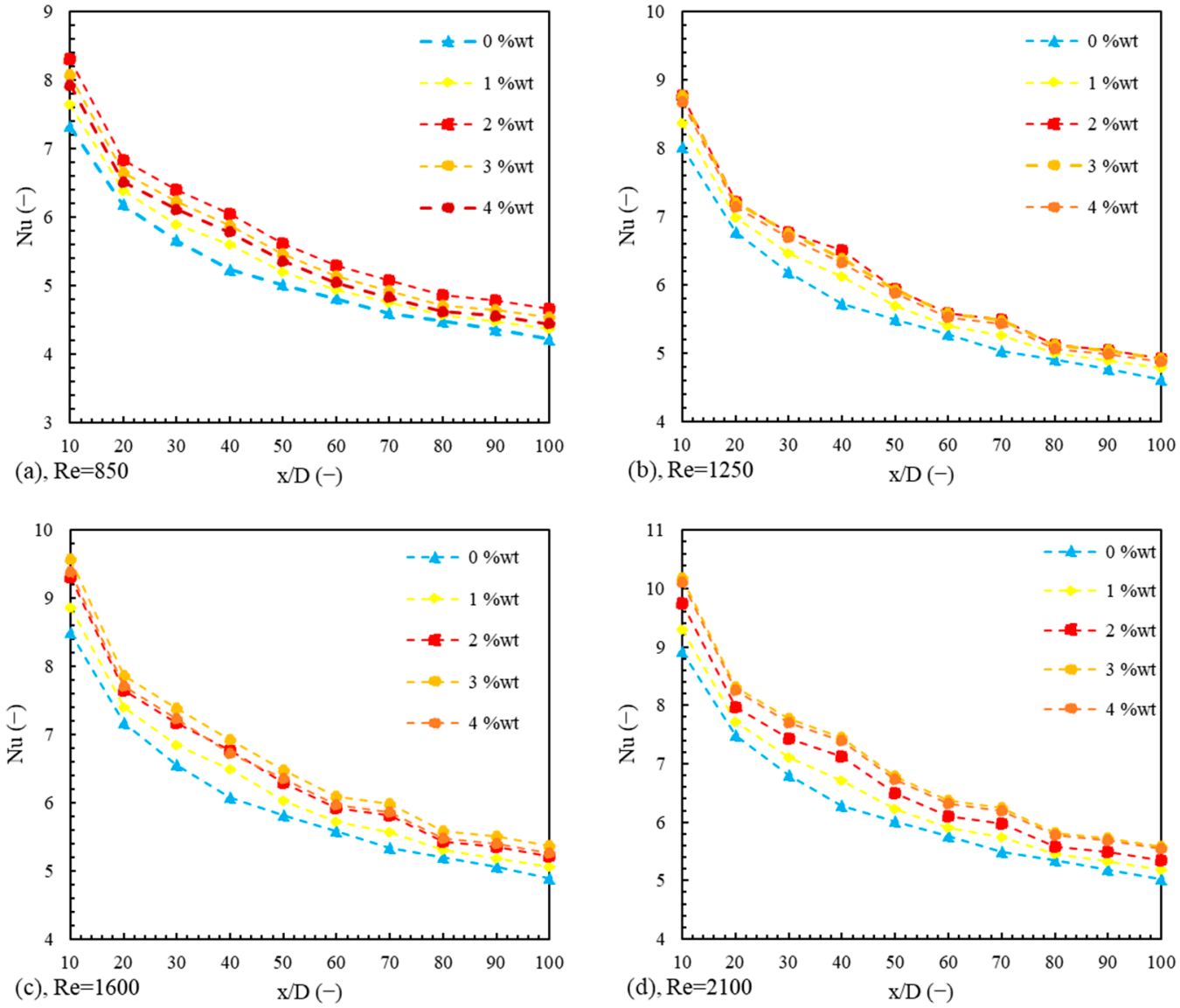

Figure 10. The results of local *Nu* for rectangular cross-section with different nanoparticle concentrations in (**a**) *Re* = 850, (**b**) *Re* = 1250, (**c**) *Re* = 1600, and (**d**) *Re* = 2100.

In the following, we examine the average values in different situations.

6.1.4. Average Nusselt Number

Figure 11 shows the average *Nu* number at different *Re* numbers. One of the effective elements affecting the average *Nu* number is thermal conductivity. The increase in this parameter would increase the HTC and, as a result, the average *Nu* number [69–71]. Comparing different cross-sectional surfaces shows that circular surfaces' average *Nu* number is higher. According to Figure 11a, in the *Re* number of 850, nanofluid with 2% concentration has the highest value, 6.67, which is 15% higher than the rectangular cross-section and 20% higher than the square cross-section. According to Figure 11b, at Re 1250, the nanofluid with 2% concentration has the highest value in the circular state. In this flow, the circular mode is 16% higher than the rectangular section and 20% higher than the square section.

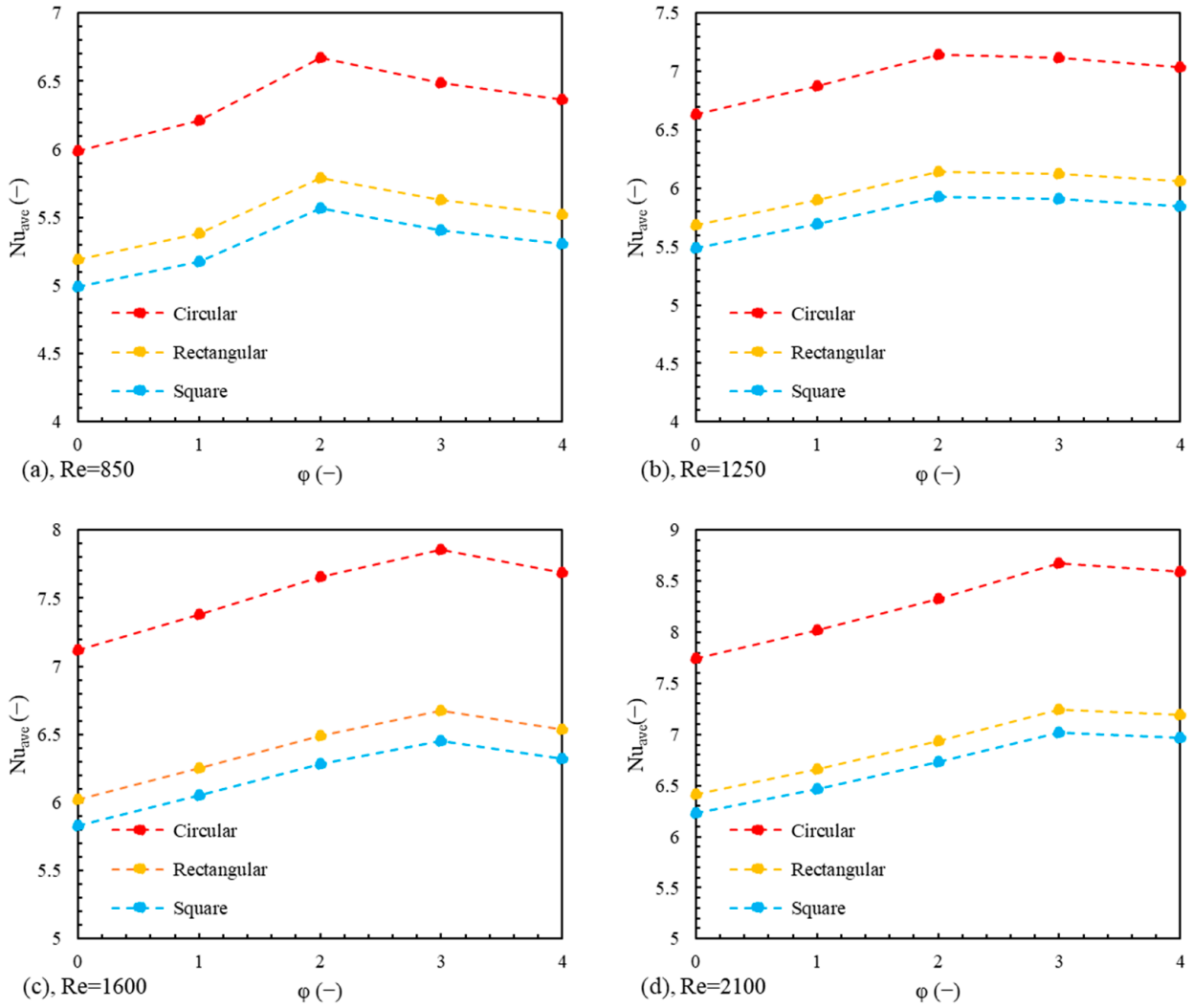

Figure 11. The average *Nu* number for all cross-sections in different fluid flows in (**a**) *Re* = 850, (**b**) *Re* = 1250, (**c**) *Re* = 1600, and (**d**) *Re* = 2100.

It should be noted that the *Nu* number of nanofluid at *Re* number 1250 is equal to 7.14, which has increased by 7% compared to the *Re* number 850, which was equal to 6.67. In Re 1600 and 2100, the highest average *Nu* value is in nanofluid with a concentration of 3% in the circular section. The maximum average *Nu* number is 7.85 at 1600 Re and 8.67 at 2100 *Re* numbers. It should also be noted that as the *Re* number increases, the *Nu* number also increases. The effective thermal conductivity enhancement nanofluid may be credited for the first improvement in *Nu* number since the HTC is proportional to thermal conductivity. Additionally, according to the experimental findings, nanoparticles in the flow impact heat transfer beyond what would be predicted by having more thermal conductivity. As a result, thermal conductivity augmentation has little impact on the enhancement of convective HTC. Furthermore, thermal conductivity in dynamic conditions may be significantly higher than in static conditions. The viscosity and thermal conductivity of near-surface nanofluids are dramatically increased by particle migration toward the centerline of a tube as a result of Brownian diffusion and thermophoresis. The viscosity and thermal conductivity of nanofluids close to the centerline are dramatically increased by particle migration into the tube's centerline caused by Brownian diffusion and thermophoresis. The velocity profile flattens due to the nanofluids' increased viscosity close to the centerline. Under a constant heat flux, the flattened velocity profile reduces the gap between the bulk mean temperature of nanofluids and the average tube wall temperature.

Figure 12 shows the trend of the average *Nu* number in pure water and nanofluid with concentrations of 1%, 2%, 3%, and 4%.

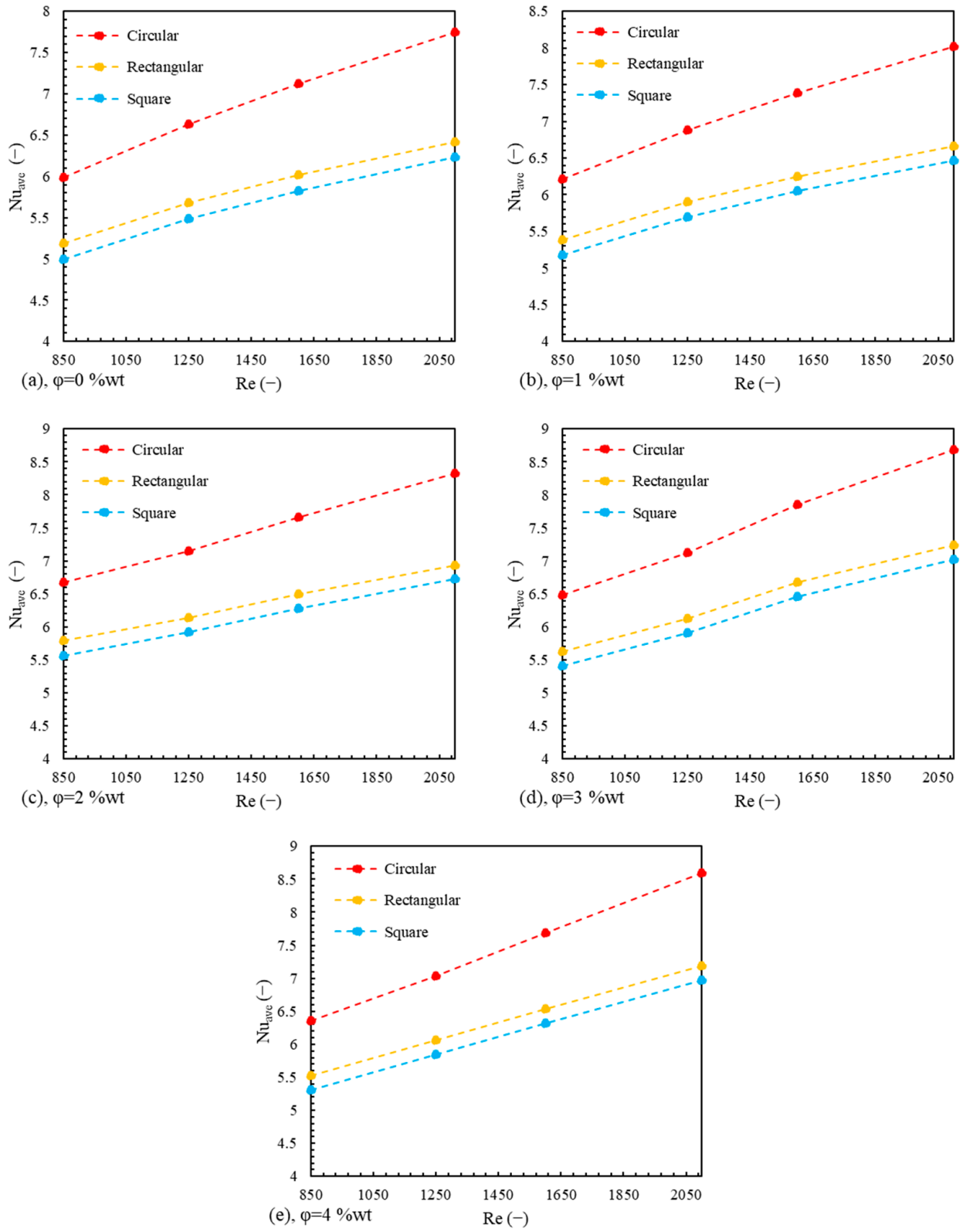

Figure 12. The average *Nu* number in all cross-sections within a range of *Re* numbers for (**a**) water, (**b**) nanofluid with 1% concentration, (**c**) nanofluid with 2% concentration, (**d**) nanofluid with 3% concentration, and (**e**) nanofluid with 4% concentration.

6.2. Entropy Generation Analysis

The analysis of entropy production for all three sections in different *Re* numbers and different fluids is shown in Figure 13. As mentioned earlier, the total entropy generation comprises two components: thermal and frictional. The frictional term is not significant in laminar flows and mainly lower *Re* numbers, but the thermal component is dominant. As the *Re* number increases, the pressure drop would increase, increasing the frictional term of entropy generation. To summarize, there are two variations in the tests. The effects of two variations on the frictional and thermal components of the entropy generation are discussed in the following. Increasing the *Re* number would affect the thermal and frictional terms positively and negatively, respectively. In other words, by increasing the *Re* number, the thermal performance would enhance, and therefore, the thermal entropy generation decreases. By doing this, however, the frictional entropy generation would increase due to the increase in pressure drop. Moreover, the addition of nanoparticles would similarly affect the entropy generation. Adding more nanoparticles to the flow would increase the thermal performance due to thermal conductivity enhancement, better migration of particles, and lower thermal boundary layer thickness. This would lead to a lower thermal entropy generation in the flow. However, the nanoparticle addition would negatively impact the frictional term of the entropy generation by increasing the pressure drop. Regarding the cross-sections, the rectangular one has the highest entropy generation. This contrasts with the thermal performance, where the square had the poorest performance. This swap is probably due to the pressure drop in the rectangular cross-section. Since the square cross-section benefits symmetry on all sides, the lack of this symmetry in the rectangular cross-section may have caused more frictional entropy generation. As a result, the total entropy generation of the rectangular cross-section is the highest, and the circular cross-section has the lowest total entropy generation.

Considering that the circular cross-section has a higher thermal performance, the thermal term of its entropy production is much lower than the other two sections. As a result, it has a lower total entropy production. At low *Re* numbers, the thermal term of entropy production dominates, but the frictional term also becomes important as the *Re* number increases. This issue is also clear in Figure 13c. In general, adding nanoparticles and increasing the *Re* number causes a decrease in entropy production. Moreover, the entropy production in the circular cross-section is less than in the other two sections. The difference in entropy generation for $Re = 2100$ in all fluids is presented in the following. Based on Figure 13a, the entropy generation of the circular cross-section is 41.89% lower than that of the rectangular cross-section. The square cross-section has 8.95% lower entropy generation than the rectangular cross-section. In Figure 13b, circular and square cross-sections have 41.86% and 8.3% lower entropy generation compared to rectangular cross-sections. The amount of entropy generation, in general, has decreased by adding nanoparticles. This is probably because of the thermal boost provided by the nanoparticle addition. Figure 13c shows the results for 3% nanofluid, and the entropy generations' difference compared to rectangular cross-sections in $Re = 2100$ is 41.69% and 8.49% for circular and square cross-sections, respectively. The results of Figure 13d reveal that the differences in circular and square cross-sections compared to the rectangular one are 41.4% and 8.28%, respectively. In Figure 13e, the circular cross-section has 41.52% lower entropy generation, and that of the square is 8.01% compared to the rectangular cross-section. By adding more nanoparticles to the base fluid, the total entropy generation decreases slightly, but this does not significantly affect the deficit among different cross-sections in laminar flow. A similar trend is observed in [72].

Based on Figure 14, the lowest entropy generation is achieved in 2% nanofluid in lower *Re* numbers. However, as the *Re* number increases, the nanoparticle addition would continue to lower the entropy generation. In Figure 14a, the lowest entropy generation is on 2% nanoparticle concentration. This figure shows that using the circular cross-section would decrease the entropy generation by 39.48% compared to the rectangular cross-section. The square cross-section has a 7.76% lower entropy generation than the rectangular cross-

section. In Figure 14b, however, the best results are observed in $\varphi = 4$, where the circular and square cross-sections have 39.78% and 7.52% improvement compared to rectangular case. In Figure 14c,d, the same trends are observed, where the lowest entropy generation is at 4% nanofluid. The cross-sections' differences are also in the same range as the previous figures. Nevertheless, as the *Re* number increases, the entropy generation decreases. Based on the entropy generation analysis, the best case is observed in the circular cross-section of $Re = 2100$ in the nanofluid with 4% nanoparticle concentration at 1.39 W/K. The study of Kurnia et al. [73] showed the same trend.

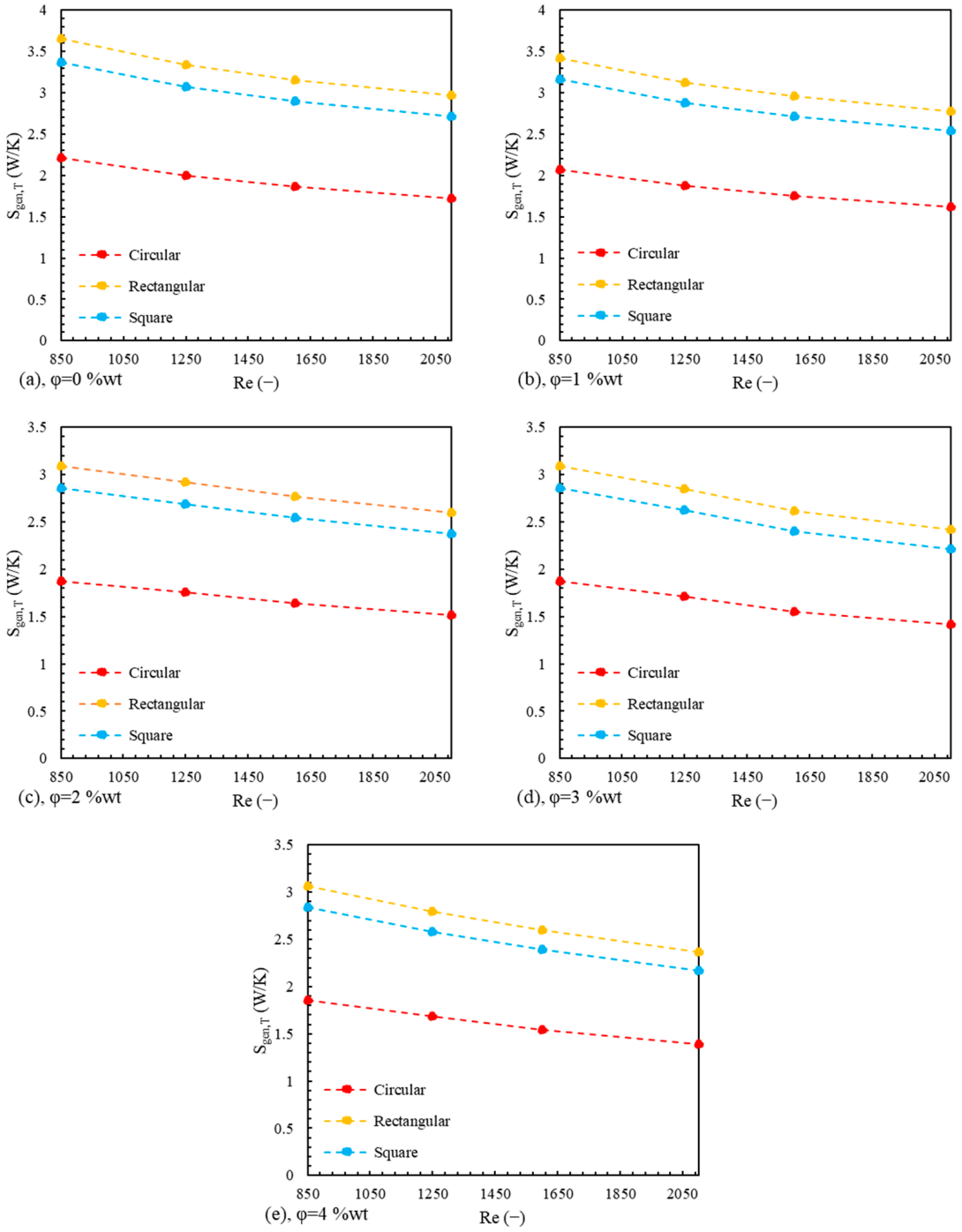

Figure 13. Total entropy generation of all cross-sections in a range of *Re* numbers for (**a**) water, (**b**) nanofluid with 1% concentration, (**c**) nanofluid with 2% concentration, (**d**) nanofluid with 3% concentration, and (**e**) nanofluid with 4% concentration.

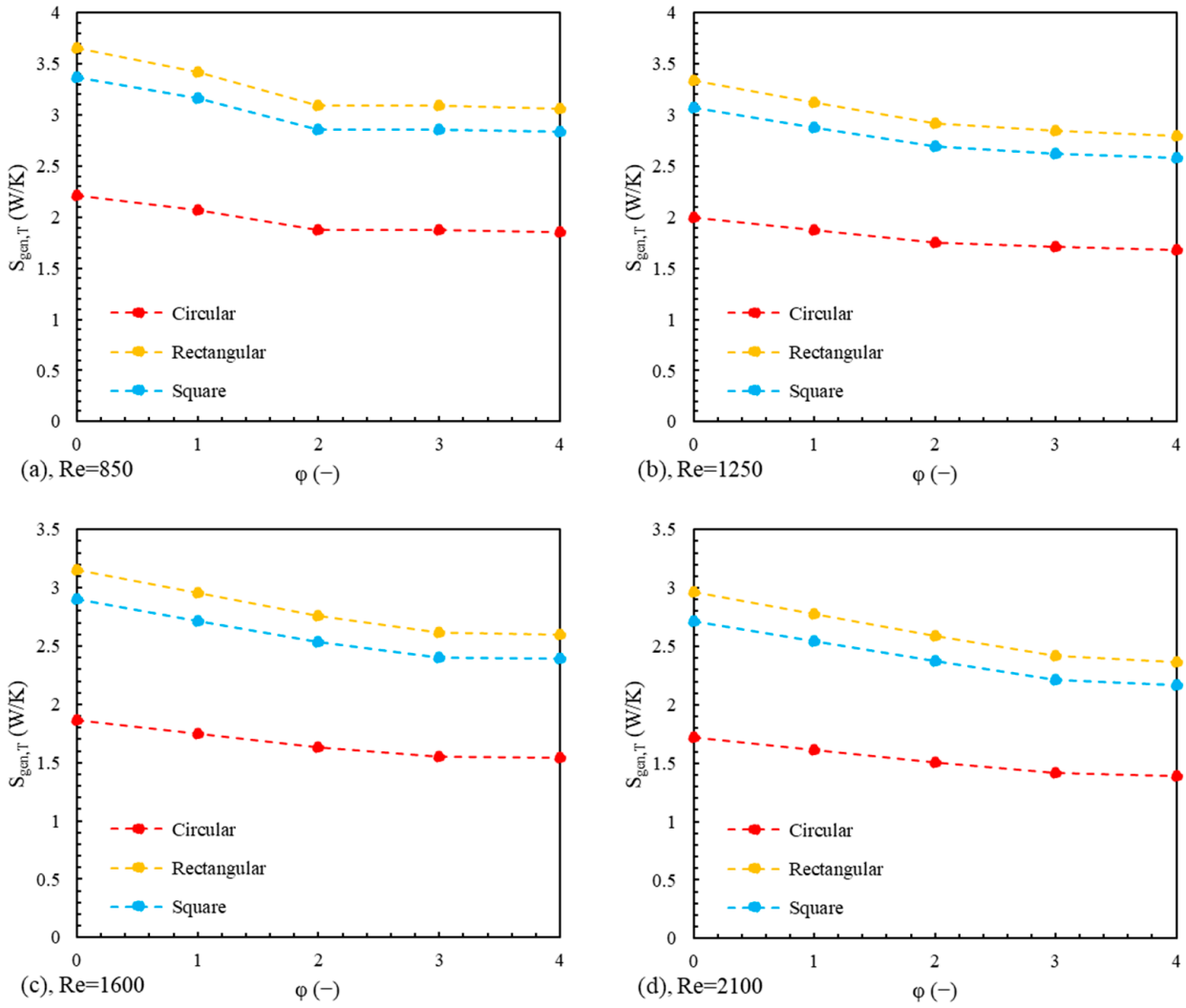

Figure 14. Total entropy generation in all cross-sections for different fluids in (**a**) *Re* = 850, (**b**) *Re* = 1250, (**c**) *Re* = 1600, and (**d**) *Re* = 2100.

However, nanofluid stability is another factor that needs to be considered. Surfactant is used to increase the stability of nanofluid and prevent the nanoparticles from being clustered. This clustering could reduce the thermal performance of the fluid through two mechanisms. The first is that the nanofluid loses the increased thermal properties and the wettability decreases. Moreover, they cause thermal resistance that could decrease the Nusselt number and increase the entropy generation.

7. Conclusions

In this study, we investigated the effects of various types of cross-sections on the thermal performance of a heat transfer system. The effect of adding nanoparticles to the base fluid was also investigated. In addition, the effect of increasing the *Re* number on the *Nu* number was investigated. Total entropy production was investigated in this study. The results obtained from the experiments show that the highest value of the local and average *Nu* number was observed in the tube with a circular cross-section. The rectangular section had the highest thermal performance after the circular section. Finally, the square cross-section had the lowest thermal performance among the examined sections. The difference in thermal performance of the three cross-sections is such that, on average, in all points of the tube under the same conditions, the circular cross-section was 15–30% higher than the rectangular cross-section and 20–35% higher than the square cross-section. Based

on the thermal analysis, the best case in $Re = 850$ and $Re = 1250$ is at nanofluid with 2% nanoparticle concentration. In contrast, at higher *Re* numbers, the thermal performance increases with the increase in nanofluid concentration, and the best case is at nanofluid with 4% nanoparticle concentration. Entropy generation was also investigated in this study, and the total average entropy produced decreased with the increase in the *Re* number. Entropy production was from the largest to the smallest in rectangular, square, and circular cross-sections. The enhancement due to the cross-sections for circular one was 37–42% compared to rectangular cross-sections. The square cross-section had 7–9.5% enhancement compared to the rectangular cross-section. The addition of nanoparticles also decreased entropy production. Finally, according to the thermal analysis, the best *Nu* was observed in nanofluid with 2% concentration in lower *Re* numbers. Nevertheless, the best thermal performance in higher *Re* numbers was in nanofluids with 4% concentration. The entropy generation analysis best case is in nanofluid with 4% nanoparticle concentration. Among all cross-sections, the circular cross-section seems to outperform the others in both thermal and entropy generation analyses. For further research in this area, other cross-sections such as coils, ducts, and triangular could be considered, and a comparison should be made between circular and other cross-sections. Moreover, recently, as the use of machine learning algorithms for predicting parameters is becoming common, other research could be devoted to proposing predictive models.

Author Contributions: A.E.J., M.S., B.D. and V.S.: Conceptualization, methodology, software, formal analysis, investigation, data curation, validation, writing—original draft and reviewing, visualization. P.S.: Conceptualization, formal analysis, software, investigation, resources, data curation, writing—review and editing. M.A.J.M.: Conceptualization, resources, project administration, software. All authors have read and agreed to the published version of the manuscript.

Funding: This research was funded by King Khalid University, Abha, Saudi Arabia, grant number GRP. 2/37/43.

Data Availability Statement: The data presented in this study are available on request from the corresponding author.

Acknowledgments: This work was supported by the King Khalid University, Abha, Saudi Arabia. The authors extend their appreciation to the King Khalid University for funding this work through the Larg Groups Project under grant number (R.G.P. 2/37/43). We would like to offer a warm thanks to the teams from the University of Montenegro and Comenius University Bratislava for administrative and technical support.

Conflicts of Interest: The authors declare that they have no known competing financial interest or personal relationships that could have appeared to influence the work reported in this paper.

Nomenclature

A	The area of heat transfer (m^2)
C_p	Specific heat of the fluid (J kg^{-1} K^{-1})
d & D	Diameter (m)
f	Friction factor
g	Gravitational constant (m s^{-2})
I	Current (A)
k	Conductivity (W $m^{-2}K^{-1}$)
M	Molar concentration
$\dot{m}$	Mass flux (kg m^{-2} s^{-1})
Nu	Nusselt number
P	Peripheral (m^2)
q''	Heat flux (W m^{-2})
Re	Reynolds number
S	Entropy
T	Temperature (K)

v	Velocity (m s^{-1})
V	Voltage (V)
X	Entrance length (m)
Greek letters	
δ	Uncertainty
μ	Viscosity (Pa.s)
ρ	Density (kg m^{-3})
φ	Nanoparticle concentration
Subscripts	
act	Actual
ave	Average
el	Electrical
gen	Generation
loss	Loss
T	Total

References

1. Bejan, A. A Study of Entropy Generation in Fundamental Convective Heat Transfer. *J. Heat Transf.* **1979**, *101*, 718–725. [CrossRef]
2. Bejan, A. Entropy generation minimization: The new thermodynamics of finite-size devices and finite-time processes. *J. Appl. Phys.* **1996**, *79*, 1191–1218. [CrossRef]
3. Sahin, A.Z.; Ben-Mansour, R. Entropy generation in laminar fluid flow through a circular pipe. *Entropy* **2003**, *5*, 404–416. [CrossRef]
4. Alimoradi, H.; Eskandari, E.; Pourbagian, M.; Shams, M. A parametric study of subcooled flow boiling of Al2O3/water nanofluid using numerical simulation and artificial neural networks. *Nanoscale Microscale Thermophys. Eng.* **2022**, *26*, 129–159. [CrossRef]
5. Cui, W.; Li, X.; Li, X.; Si, T.; Lu, L.; Ma, T.; Wang, Q. Thermal performance of modified melamine foam/graphene/paraffin wax composite phase change materials for solar-thermal energy conversion and storage. *J. Clean. Prod.* **2022**, *367*, 133031. [CrossRef]
6. Majid, S.; Mohammad, J. Optimal selection of annulus radius ratio to enhance heat transfer with minimum entropy generation in developing laminar forced convection of water-Al_2O_3 nanofluid flow. *J. Cent. South Univ.* **2017**, *24*, 850–1865. [CrossRef]
7. Zaboli, S.; Alimoradi, H.; Shams, M. Numerical investigation on improvement in pool boiling heat transfer characteristics using different nanofluid concentrations. *J. Therm. Anal. Calorim.* **2022**, *147*, 10659–10676. [CrossRef]
8. Zhong, Q.; Chen, Y.; Zhu, B.; Liao, S.; Shi, K. A temperature field reconstruction method based on acoustic thermometry. *Measurement* **2022**, *200*, 111642. [CrossRef]
9. Roodbari, M.; Alimoradi, H.; Shams, M.; Aghanajafi, C. An experimental investigation of microstructure surface roughness on pool boiling characteristics of TiO_2 nanofluid. *J. Therm. Anal. Calorim.* **2022**, *147*, 3283–3298. [CrossRef]
10. Shahsavar, A.; Entezari, S.; Askari, I.B.; Jamei, M.; Karbasi, M.; Shahmohammadi, M. Investigation on two-phase fluid mixture flow, heat transfer and entropy generation of a non-Newtonian water-CMC/CuO nanofluid inside a twisted tube with variable twist pitch: Numerical and evolutionary machine learning simulation. *Eng. Anal. Bound. Elem.* **2022**, *140*, 322–337. [CrossRef]
11. Alimoradi, H.; Soltani, M.; Shahali, P.; Moradi Kashkooli, F.; Larizadeh, R.; Raahemifar, K.; Adibi, M.; Ghasemi, B. Experimental investigation on improvement of wet cooling tower efficiency with diverse packing compaction using ANN-PSO algorithm. *Energies* **2022**, *14*, 167. [CrossRef]
12. Huminic, G.; Huminic, A. A numerical approach on hybrid nanofluid behavior in laminar duct flow with various cross sections. *J. Therm. Anal. Calorim.* **2020**, *140*, 2097–2110. [CrossRef]
13. Alimoradi, H.; Shams, M.; Ashgriz, N.; Bozorgnezhad, A. A novel scheme for simulating the effect of microstructure surface roughness on the heat transfer characteristics of subcooled flow boiling. *Case Stud. Therm. Eng.* **2021**, *24*, 100829. [CrossRef]
14. Dalir, N. Numerical study of entropy generation for forced convection flow and heat transfer of a Jeffrey fluid over a stretching sheet. *Alex. Eng. J.* **2014**, *53*, 769–778. [CrossRef]
15. Biswal, P.; Basak, T. Entropy generation based approach on natural convection in enclosures with concave/convex side walls. *Int. J. Heat Mass Transf.* **2015**, *82*, 213–235. [CrossRef]
16. Nazeryan, M.; Lakzian, E. Detailed entropy generation analysis of a Wells turbine using the variation of the blade thickness. *Energy* **2018**, *143*, 385–405. [CrossRef]
17. Delouei, A.A.; Atashafrooz, M.; Sajjadi, H.; Karimnejad, S. The thermal effects of multi-walled carbon nanotube concentration on an ultrasonic vibrating finned tube heat exchanger. *Int. Commun. Heat Mass Transf.* **2022**, *135*, 106098. [CrossRef]
18. Delouei, A.A.; Sajjadi, H.; Izadi, M.; Mohebbi, R. The simultaneous effects of nanoparticles and ultrasonic vibration on inlet turbulent flow: An experimental study. *Appl. Therm. Eng.* **2019**, *146*, 268–277. [CrossRef]
19. Guo, Z.; Tian, X.; Wu, Z.; Yang, J.; Wang, Q. Heat transfer of granular flow around aligned tube bank in moving bed: Experimental study and theoretical prediction by thermal resistance model. *Energy Convers. Manag.* **2022**, *257*, 115435. [CrossRef]
20. Noghrehabadi, A.; Saffarian, M.R.; Pourrajab, R.; Ghalambaz, M. Entropy analysis for nanofluid flow over a stretching sheet in the presence of heat generation/absorption and partial slip. *J. Mech. Sci. Technol.* **2013**, *27*, 927–937. [CrossRef]
21. Wang, T.; Huang, Z.; Xi, G. Entropy generation for mixed convection in a square cavity containing a rotating circular cylinder using a local radial basis function method. *Int. J. Heat Mass Transf.* **2017**, *106*, 1063–1073. [CrossRef]

22. Zhou, Y.; Zhu, L.; Yu, J.; Li, Y. Optimization of plate-fin heat exchangers by minimizing specific entropy generation rate. *Int. J. Heat Mass Transf.* **2014**, *78*, 942–946. [CrossRef]
23. Falahat, A.; Shabani, M.; Saffarian, M.R. Entropy generation of pseudo-plastic non-Newtonian nanofluids in circular duct under constant wall temperature. *J. Mech. Eng. Technol.* **2018**, *10*, 1–10.
24. Shiravi, A.H.; Shafiee, M.; Firoozzadeh, M.; Bostani, H.; Bozorgmehrian, M. Experimental study on convective heat transfer and entropy generation of carbon black nanofluid turbulent flow in a helical coiled heat exchanger. *J. Therm. Anal. Calorim.* **2021**, *145*, 597–607. [CrossRef]
25. Kadivar, M.; Sharifpur, M.; Meyer, J.P. Convection heat transfer, entropy generation analysis and thermodynamic optimization of nanofluid flow in spiral coil tube. *Heat Transf. Eng.* **2021**, *42*, 1573–1589. [CrossRef]
26. Saffarian, M.R.; Bahoosh, R.; Doranehgard, M.H. Entropy generation in the intake pipe of an internal combustion engine. *Eur. Phys. J. Plus* **2019**, *134*, 476. [CrossRef]
27. Tuncer, A.D.; Sözen, A.; Khanlari, A.; Gürbüz, E.Y.; Variyenli, H.İ. Upgrading the performance of a new shell and helically coiled heat exchanger by using longitudinal fins. *Appl. Therm. Eng.* **2021**, *191*, 116876. [CrossRef]
28. Cui, W.; Si, T.; Li, X.; Li, X.; Lu, L.; Ma, T.; Wang, Q. Heat transfer analysis of phase change material composited with metal foam-fin hybrid structure in inclination container by numerical simulation and artificial neural network. *Energy Rep.* **2022**, *8*, 10203–10218. [CrossRef]
29. Xiong, Q.; Izadi, M.; Shehzad, S.A.; Mohammed, H.A. 3D numerical study of conical and fusiform turbulators for heat transfer improvement in a double-pipe heat exchanger. *Int. J. Heat Mass Transf.* **2021**, *170*, 120995. [CrossRef]
30. Qu, M.; Liang, T.; Hou, J.; Liu, Z.; Yang, E.; Liu, X. Laboratory study and field application of amphiphilic molybdenum disulfide nanosheets for enhanced oil recovery. *J. Petroleum Sci. Eng.* **2022**, *208*, 109695. [CrossRef]
31. Tran, N.; Liaw, J.S.; Wang, C.C. Performance of thermofluidic characteristics of recuperative wavy-plate heat exchangers. *Int. J. Heat Mass Transf.* **2021**, *170*, 121027. [CrossRef]
32. Gasmia, A.; Elboughdirib, N.; Ghernaoutb, D.; Hannachia, A.; Halimb, K.A.; Khanf, M.I. Electrocoagulation process for removing dyes and chemical oxygen demand from wastewater: Operational conditions and economic assessment—A review. *Desalination Water Treat.* **2022**, *271*, 74–107. [CrossRef]
33. Zheng, D.; Yang, J.; Wang, J.; Kabelac, S.; Sundén, B. Analyses of thermal performance and pressure drop in a plate heat exchanger filled with ferrofluids under a magnetic field. *Fuel* **2021**, *293*, 120432. [CrossRef]
34. Zhao, Y.; Wang, Z. Subset simulation with adaptable intermediate failure probability for robust reliability analysis: An unsupervised learning-based approach. *Struct. Multidiscip. Optim.* **2022**, *65*, 1–22. [CrossRef]
35. Zhao, Y.; Foong, L.K. Predicting Electrical Power Output of Combined Cycle Power Plants Using a Novel Artificial Neural Network Optimized by Electrostatic Discharge Algorithm. *Measurement* **2022**, *198*, 111405. [CrossRef]
36. Al Omari, S.A.B.; Ghazal, A.M.; Elnajjar, E.; Qureshi, Z.A. Vibration-enhanced direct contact heat exchange using gallium as a solid phase change material. *Int. Commun. Heat Mass Transf.* **2021**, *120*, 104990. [CrossRef]
37. Zhao, Y.; Hu, H.; Song, C.; Wang, Z. Predicting compressive strength of manufactured-sand concrete using conventional and metaheuristic-tuned artificial neural network. *Measurement* **2022**, *194*, 110993. [CrossRef]
38. Foong, L.K.; Zhao, Y.; Bai, C.; Xu, C. Efficient metaheuristic-retrofitted techniques for concrete slump simulation. *Smart Struct. Syst. Int. J.* **2021**, *27*, 745–759.
39. Shahsavar, A.; Bakhshizadeh, M.A.; Arici, M.; Afrand, M.; Rostami, S. Numerical study of the possibility of improving the hydrothermal performance of an elliptical double-pipe heat exchanger through the simultaneous use of twisted tubes and non-Newtonian nanofluid. *J. Therm. Anal. Calorim.* **2021**, *143*, 2825–2840. [CrossRef]
40. Wu, P.; Liu, A.; Fu, J.; Ye, X.; Zhao, Y. Autonomous surface crack identification of concrete structures based on an improved one-stage object detection algorithm. *Eng. Struct.* **2022**, *272*, 114962. [CrossRef]
41. Zhao, Y.; Zhong, X.; Foong, L.K. Predicting the splitting tensile strength of concrete using an equilibrium optimization model. *Steel Compos. Struct. Int. J.* **2021**, *39*, 81–93.
42. Alimoradi, H.; Zaboli, S.; Shams, M. Numerical simulation of surface vibration effects on improvement of pool boiling heat transfer characteristics of nanofluid. *Korean J. Chem. Eng.* **2022**, *39*, 69–85. [CrossRef]
43. Eskandari, E.; Alimoradi, H.; Pourbagian, M.; Shams, M. Numerical investigation and deep learning-based prediction of heat transfer characteristics and bubble dynamics of subcooled flow boiling in a vertical tube. *Korean J. Chem. Eng.* **2022**, *39*, 3227–3245. [CrossRef]
44. Alimoradi, H.; Shams, M.; Ashgriz, N. Enhancement in the Pool Boiling Heat Transfer of Copper Surface by Applying Electrophoretic Deposited Graphene Oxide Coatings. *Int. J. Multiph. Flow* **2022**, *159*, 104350. [CrossRef]
45. Zhao, Y.; Yan, Q.; Yang, Z.; Yu, X.; Jia, B. A novel artificial bee colony algorithm for structural damage detection. *Adv. Civil Eng.* **2020**, *2020*, 3743089. [CrossRef]
46. Dzyubenko, B.V. Influence of flow twisting on convective heat transfer in banks of twisted tubes. *Heat Transf. Res.* **2005**, *36*, 449–460. [CrossRef]
47. Zhang, X.X.; Wei, G.H.; Sang, Z.F. Experimental research of heat transfer and flow friction properties in twisted tube heat exchanger. *Huaxue Gongcheng Chem. Eng.* **2007**, *35*, 17–20.
48. Qing, D.F.; Duan, X.; Liu, Y.H. Experimental investigation on running characteristics of twisted tube in evaporator. *Chem. Eng.* **2008**, *36*, 12–15.

49. Yu, Y.; Zhu, D.S.; Zeng, L.D.; Zou, J. Experimental investigation on heat transfer enhancement of twisted tube. *Chem. Eng.* **2015**, *39*, 18–21.
50. Samruaisin, P.; Kunlabud, S.; Kunnarak, K.; Chuwattanakul, V.; Eiamsa-Ard, S. Intensification of convective heat transfer and heat exchanger performance by the combined influence of a twisted tube and twisted tape. *Case Stud. Therm. Eng.* **2019**, *14*, 100489. [CrossRef]
51. Choi, S.U.; Eastman, J.A. *Enhancing Thermal Conductivity of Fluids with Nanoparticles*; No. ANL/MSD/CP-84938; CONF-951135-29; Argonne National Lab. ANL: Argonne, IL, USA, 1995.
52. Zhao, Y.; Joseph, A.J.J.M.; Zhang, Z.; Ma, C.; Gul, D.; Schellenberg, A.; Hu, N. Deterministic snap-through buckling and energy trapping in axially-loaded notched strips for compliant building blocks. *Smart Mater. Struct.* **2020**, *29*, 02LT03. [CrossRef]
53. Alimoradi, H.; Shams, M.; Ashgriz, N. Bubble behavior and nucleation site density in subcooled flow boiling using a novel method for simulating the microstructure of surface roughness. *Korean J. Chem. Eng.* **2022**, *39*, 2945–2958. [CrossRef]
54. Zhao, Y.; Hu, H.; Bai, L.; Tang, M.; Chen, H.; Su, D. Fragility analyses of bridge structures using the logarithmic piecewise function-based probabilistic seismic demand model. *Sustainability* **2021**, *13*, 7814. [CrossRef]
55. Bretado-de los Rios, M.S.; Rivera-Solorio, C.I.; Nigam, K.D.P. An overview of sustainability of heat exchangers and solar thermal applications with nanofluids: A review. *Renew. Sustain. Energy Rev.* **2021**, *142*, 110855. [CrossRef]
56. Khoshvaght-Aliabadi, M.; Arani, Z.; Rahimpour, F. Influence of Al_2O_3–H_2O nanofluid on performance of twisted minichannels. *Adv. Powder Technol.* **2016**, *27*, 1514–1525. [CrossRef]
57. Feizabadi, A.; Khoshvaght-Aliabadi, M.; Rahimi, A.B. Numerical investigation on Al_2O_3/water nanofluid flow through twisted-serpentine tube with empirical validation. *Appl. Therm. Eng.* **2018**, *137*, 296–309. [CrossRef]
58. Omidi, M.; Rabienataj Darzi, A.A.; Farhadi, M. Turbulent heat transfer and fluid flow of alumina nanofluid inside three-lobed twisted tube. *J. Therm. Anal. Calorim.* **2019**, *137*, 1451–1462. [CrossRef]
59. Mahato, S.K.; Rana, S.C.; Barman, R.N.; Goswami, S. Numerical analysis of heat transfer and fluid flow through the twisted square duct (TSD): Nanofluid as working fluid. *J. Mech. Sci. Technol.* **2019**, *33*, 5507–5514. [CrossRef]
60. Zohuri, B.; McDaniel, P. First law of thermodynamics. In *Thermodynamics in Nuclear Power Plant Systems*; Springer: Cham, Switzerland, 2019; pp. 99–148.
61. Erguvan, M.; MacPhee, D.W. Second law optimization of heat exchangers in waste heat recovery. *Int. J. Energy Res.* **2019**, *43*, 5714–5734. [CrossRef]
62. Rashidi, S.; Javadi, P.; Esfahani, J.A. Second law of thermodynamics analysis for nanofluid turbulent flow inside a solar heater with the ribbed absorber plate. *J. Therm. Anal. Calorim.* **2019**, *135*, 551–563. [CrossRef]
63. Zhao, Y.; Moayedi, H.; Bahiraei, M.; Foong, L.K. Employing TLBO and SCE for optimal prediction of the compressive strength of concrete. *Smart Struct. Syst.* **2020**, *26*, 753–763.
64. Yan, B.; Ma, C.; Zhao, Y.; Hu, N.; Guo, L. Geometrically Enabled Soft Electroactuators via Laser Cutting. *Adv. Eng. Mater.* **2015**, *21*, 1900664. [CrossRef]
65. Goharkhah, M.; Salarian, A.; Ashjaee, M.; Shahabadi, M. Convective heat transfer characteristics of magnetite nanofluid under the influence of constant and alternating magnetic field. *Powder Technol.* **2015**, *274*, 258–267. [CrossRef]
66. Ratts, E.B.; Raut, A.G. Entropy generation minimization of fully developed internal flow with constant heat flux. *J. Heat Transf.* **2004**, *126*, 656–659. [CrossRef]
67. Hesselgreaves, J.E. Rationalisation of second law analysis of heat exchangers. *Int. J. Heat Mass Transf.* **2000**, *43*, 4189–4204. [CrossRef]
68. Sundar, L.S.; Naik, M.T.; Sharma, K.V.; Singh, M.K.; Reddy, T.C.S. Experimental investigation of forced convection heat transfer and friction factor in a tube with Fe_3O_4 magnetic nanofluid. *Exp. Therm. Fluid Sci.* **2012**, *37*, 65–71. [CrossRef]
69. Sohn, C.W.; Chen, M.M. Microconvective thermal conductivity in disperse two-phase mixtures as observed in a low velocity Couette flow experiment. *J. Heat Transf.* **1981**, *103*, 47–51. [CrossRef]
70. Shin, S.; Lee, S.H. Thermal conductivity of suspensions in shear flow fields. *Int. J. Heat Mass Transf.* **2000**, *43*, 4275–4284. [CrossRef]
71. Phillips, R.J.; Armstrong, R.C.; Brown, R.A.; Graham, A.L.; Abbott, J.R. A constitutive equation for concentrated suspensions that accounts for shear-induced particle migration. *Phys. Fluids A Fluid Dyn.* **1992**, *4*, 30–40. [CrossRef]
72. Jankowski, T.A. Minimizing entropy generation in internal flows by adjusting the shape of the cross-section. *Int. J. Heat Mass Transf.* **2009**, *52*, 3439–3445. [CrossRef]
73. Kurnia, J.C.; Sasmito, A.P.; Shamim, T.; Mujumdar, A.S. Numerical investigation of heat transfer and entropy generation of laminar flow in helical tubes with various cross sections. *Appl. Therm. Eng.* **2016**, *102*, 849–860. [CrossRef]